Raman Spectroscopy Study on Laser-Structured Surface

ZHAO-XU YAN

December 2015

Graduate School of Engineering

Osaka University

Table of contents

Introduction

Surface plays an important role in physics, chemistry and biology [1-3]. Most of reactions happen on the substrate surface. To further improve the surface function, such as effective area in chemical reactions [4], friction coefficient in mechanical components [5], optical or electrical properties in physics [1, 6], surface-structuring technology is proved to be a vital factor. In the last decade, many different kinds of structured surfaces were designed and studied. Compared to the typical surface characterization method e.g. XPS, SEM or SPM, Raman spectroscopy is a powerful tool to study structured surface, because the vibrational fingerprint contains unique information on crystallizations, surface defects, add-molecules and atoms together with spatial information. Moreover, the method is basically non-destructive and without tagging [7, 8]. In this thesis, I have designed two types of surfaces and evaluated by Raman spectroscopy to show the usefulness of the technique for characterization of structured surfaces.

A typical challenges of structured surface is how to design effective and stable plasmonic sensor [9]. In this thesis, I present a rational design and fabrication of effective and stable metallic structures, by using laser patterning method. Combined with a simple metal decoration, two types of multilevel structures on reduced graphene oxide and black silicon were fabricated separately. Plasmonic-enhanced Raman study was carried out to judge their field enhancing performance. The Raman result showed their high electromagnetic (EM) field enhancement and stable performance as a chemical sensor with higher sensitivity.

The other challenge of structured surface is how to improve the nanoscale doping process in integrated circuits (ICs) [10]. To achieve the goal, it is crucial to understand crystal structure changes during the doping process. As a demonstration, I fabricated nanoscale doped nanostructures by FIB doping on ZnO crystal surface, which are

similar to the structures in ICs. Then Raman imaging was adopted to study the crystal lattice properties on the doped surface with spatial resolution ~300 nm. The Raman image clearly showed the distribution of crystal lattice changes at the doping area which can not be observed by scanning electron microscope or scanning probe microscope.

Thus, studying these structures is of great importance in applied physics, chemistry and biology. These results indicate that Raman holds potential for the application in micro-fabrication and semiconductor world.

Organization of this dissertation

In the 1st chapter, I introduce the basic knowledge of structured surface, including its development and challenges. Towards two typical problems, laser fabrication and FIB are introduced. In the 2nd chapter, I talk about Raman spectroscopy, from the fundamentals to its performance on plasmonic structures and FIB-structured surfaces. In the 3rd chapter, I present the fabrication and Raman characterization of Ag-RGO structures. Including the details of the laser patterning experimental and results. The Raman enhancement and signal reproducibility on the structured-surface are in detail discussed. In the 4th chapter, I report a composite Ag-black silicon structure. The results on both the enhanced Raman performance and in-situ Raman detection of catalytic reaction are presented and discussed. In the 5th chapter, I present nanoscale FIB-structured ZnO surface by Ga ion doping. It was then successfully characterized by Raman spectroscopy. Prospect and future work of tip enhanced Raman study on the nanoscale ions doped semiconductors is discussed. Finally, I finish this dissertation by a conclusion and perspective.

References:

[1]. H. Toyota, K. Takahara, M. Okano, T. Yotsuya, H. Kikuta, *Japanese Journal of Applied Physics* **40**, L747 (2001).

[2]. M. Cox, G. Ertl, R. Imbihl, *Physical review letters* **54**, 1725 (1985).

[3]. H. Toyota, K. Takahara, M. Okano, T. Yotsuya, H. Kikuta, *Japanese Journal of Applied Physics* **40**, L747 (2001).

[4]. V. Meille, *Applied Catalysis A: General* **315**, 1-17 (2006).

[5]. S. Schreck, K.-H. Zum Gahr, *Applied surface science* **247**, 616-622 (2005).

[6]. S. Matsui, Y. Ochiai, *Nanotechnology* **7**, 247 (1996).

[7]. A. C. Ferrari, *Solid state communications* **143**, 47-57 (2007).

[8]. D. A. Long, *New York*, 1-12 (1977).

[9]. A. X. Wang, X. Kong, *Materials* **8**, 3024-3052 (2015).

[10]. J. Soerensen, P. Birk, Z. Zvonar, *Wireless Personal Communications An International Journal* **17**, 291-302 (2001).

Chapter 1.

Structured surface

In this chapter, structured surface is introduced, including its fundamentals, development and challenges. To solve two typical problems in structured surface science, laser fabrication is intensely introduced in section 1.2, including its fabrication mechanism, advantages and some configurations; while in section 1.3 FIB is in detail illustrated, from its basic principles and its features in tiny surface structure fabrication.

1.1 Fundamentals of structured surface

The concept of structured surface has emerged for several decades. It has been widely studied and plays a vital role in tribology, biology and medicine, chemistry and physics [1-4]. The notion of structured surface contains several types of meaning, such as surface morphology machining, surface texturing and electrical properties tuning. There are many famous structured surfaces were developed, such as laser textured micro-dimples has been applied in mechanical seals to optimize the load capacity [5]; nanoscale doped semiconductor surfaces in microelectronics [6]; metallic nanostructures have been studied as substrate for enhancing Raman and florescence signal [7].

However, till now, there are still some challenges for the structured surface development [5, 8]. One challenge is on the metallic nanostructures, they are designed for generating strong and stable SPPs, so the satisfied structures should be relatively uniform with high level arrangement, and contain large amount of narrow metallic gaps

[9]. But by using the traditional methods (such as thermal deposition, chemical reduction), it is hard to realize this goal [10]. Because it is well known that the normal deposition methods are apt to generate random structures rather than uniform ones, no mention the desired arrangement. So it is of great importance to design an effective metallic structures for strong SPPs generation. examples

Another challenge is for the development of integrated circuits, as the feature size becomes smaller and smaller, it is difficult to follow moore's law to ulteriorly reduce it [11]. For further IC development, it is crucial to know the crystal structure changes during doping process. examples

Aimed to solve these two problems, I utilized laser patterning method and FIB for the surface structuring. Compared with other techniques (such as RIE, lithography, deposition), they could realize mask free, designable patterning with a very high efficiency. In the next sections, I will in detail introduce these two methods.

1.2 Laser technology for surface structuring

To prepare an aimed structured surface, laser fabrication technique is a remarkable one among various patterning method (such as lithography, electron beam, plasma etching). It holds many excellent features such as cost effective, easy processing, mask free and less material limitation. It has been applied for micro-nano structure in many aspects, such as design and fabrication for lithograph mask, binary optics and micro machines and so on [12-20].

The main mechanism of laser fabrication is based on photon absorption, including single photon and multi-photon absorption. Then the absorbed energy will induce the material character changes by means of thermal, mechanical and chemical effects. Used for patterning, it can be classified by single beam and multi-beam fabrication, where the former one was usually called laser direct writing (LDW) and the later one was commonly used in a form of multi-beam laser interference (MBLI). As in this thesis, I

used LDW and two beam laser interference (TBLI) patterning for the substrate preparation, in the next section, I will introduce these two methods in details. As for a SERS substrate preparation, basically a solid template is utilized, so LDW and TBLI processes are applied on solid materials. Here I mainly discuss the interaction between laser and solid material, including the fundamental theory and experimental details analysis.

Laser direct writing

For laser direct writing (LDW) on a solid material, usually a laser ablation effect is dominantly employed. Here femtosecond laser was utilized, for the extreme short pulse width makes it easy to achieve very high peak laser intensity with low pulse energies. The high peak intensity can reach the ablation threshold easily [21], while the low pulse energy makes convenient to prevent large material ablation damage. For example, a laser pulse with a pulse-width of 100 fs (10^{-13} s) and pulse energy of only 1 mJ (10^{-3} J) will have a peak intensity of $5\times10^{14}\ W/cm^2$ when focused to a 50μm diameter spot. To reach the same intensity, a 10-ns-long laser pulse has to have 100 J in a pulse.

The process of laser ablation is simple to understand. Due to the inverse Bremsstrahlung, when laser focused on the material, free electrons absorb the photon energy. Then the sorbed photon energy induces thermalization in the electron subsystem, consequently transfers to the system, and finally disperses as the electron heat pass to the target [22]. To express this process, we define the temperature of the electron subsystem and the lattice subsystem as T_e and T_l, and suppose that the electron subsystem thermalization is relatively fast, the energy transport into the solid can be expressed by the following equations [22, 23]:

$$C_e \frac{\partial T_e}{\partial t} = -\frac{\partial Q(z)}{\partial z} - \gamma\left(T_e - T_l\right) + S \tag{1.1}$$

$$C_l \frac{\partial T_l}{\partial t} = \gamma\left(T_e - T_l\right) \tag{1.2}$$

$$Q\left(z\right) = -k_e \frac{\partial T_e}{\partial z}, \quad S = I\left(t\right) A\alpha \exp\left(-\alpha z\right) \tag{1.3}$$

Where z is the direction perpendicular to the solid surface, $Q\left(z\right)$ is the heat flux, S is the term of laser heating source, $I\left(t\right)$ is the laser intensity, A is the surface transmittivity, α is the material absorption coefficient, C_e and C_l is the heat capacity of the electron and lattice subsystem respectively, γ is the electron-lattice coupling coefficient, k_e is the thermal conductivity of electron. In the above equations, as $C_e \ll C_l$, electrons could be heated very hot. When the electron energy is still smaller than its Fermi energy, the electron heat capacity is given by $C_e = C_e^{'} T_e$ (here $C_e^{'}$ is a constant) and the non-equilibrium electron thermal conductivity is $k_e = k_0\left(T_l\right) \cdot T_e / T_l$ [24, 25]. The coupling constant γ is expressed in [26] and measured by recent measurements in [25,27,28].

The above equations 1.1-1.3 have 3 characteristic time scales τ_e, τ_l and τ_L. Here $\tau_e = C_e / \gamma$, $\tau_l = C_l / \gamma$ are the electron cooling time and the lattice heating time ($\tau_e \ll \tau_l$) respectively; and τ_L is the duration of the laser pulse. As we use femtosecond laser for fabrication, $\tau_L \ll \tau_e$. For $t \ll \tau_e$, we can get $C_e T_e / t \gg \gamma T_e$, thus the coupling between electron and lattice could be ignored. In this situation Equation 1.1 can be easily solved and briefly described as follow formula:

$$T_e(t)=\left[T_0^2+\frac{2I_a\alpha}{C_e^{'}}t\exp(-\alpha z)\right]^{1/2} \tag{1.4}$$

Here $I_a=I_0A$ (I_0 is constant), and $T_0=T_e(0)$ is the original temperature. After heated by a whole laser pulse, $t=T_L$, the system temperature is much higher than the original one as $T_e(\tau_L)\gg T_0$, thus the electron temperature is illustrated as

$$T_e(\tau_L)\approx\left(\frac{2F_a\alpha}{C_e^{'}}\right)^{1/2}\exp(-z\alpha/2) \tag{1.5}$$

Here $F_a=I_a\tau_L$ is the absorbed laser fluence. Heated by a laser pulse, the electrons possess large energy and will soon shift their energy to the lattice and cool down. The obtained lattice temperature depends on the average time of the electrons cooling process as

$$T_l\approx T_e^2(\tau_L)\frac{C_e^{'}}{2C_l}\approx\frac{F_a\alpha}{C_l}\exp(-\alpha z) \tag{1.6}$$

The system evaporation threshould is defined by $\rho\Omega$, here ρ is the density, Ω is the specific evaporation heat. When the absorbed energy C_lT_l overrun the evaporation threshould, the system will be evaperated. Combined with equation 1.6, the condition for strong evaporation can be expressed as

$$F_a\geq F_{th}\exp(\alpha z) \tag{1.7}$$

where $F_{th}\approx\rho\Omega/\alpha$ is the threshold laser fluence for evaporation with femtosecond pulses. Then the ablation depth per pulse is

$$L \approx \alpha^{-1} \ln\left(F_a / F_{th}\right) \tag{1.8}$$

The femtosecond pulse laser induced ablation process could be treated as a direct solid-vapor transition, because the process time is very short. On this condition, the lattice is soon heated to vapor and rapidly expands into vacuum in a picosecond time range. As a first assumption, thermal transmition into the bulk could be neglected during all these processes. With these features, fairly precise and pure laser-solid fabrication can be realized by femtosecond laser pulses [22].

The optical setup for LDW is illustrated in Figure 1.1.

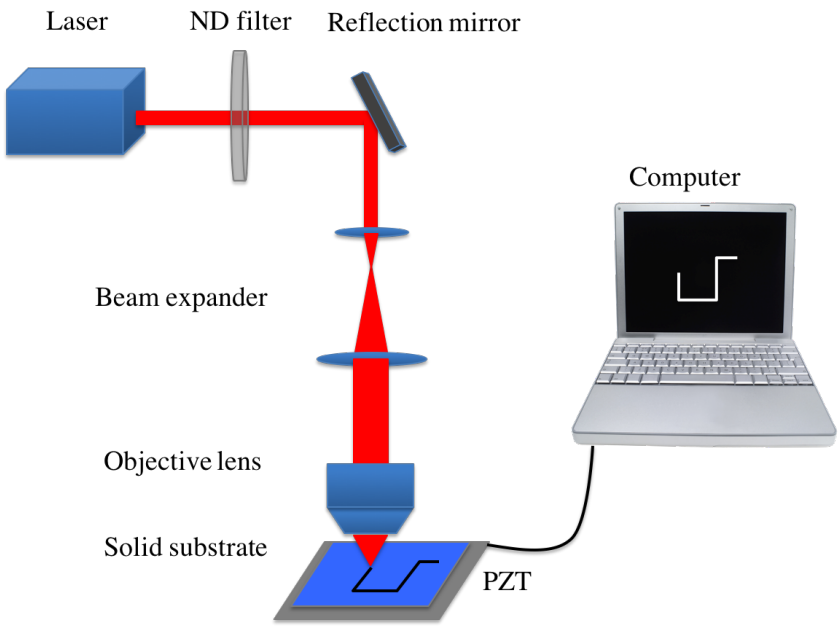

Figure 1.1 Scheme of optical setup for LDW

Normally, the laser souces used for LDW are in the infrared range, such as 780nm and 800nm wavelengths. And a ND filter is used to ajust the laser intensity. Depending on the accuracy requirement, the objective lens NA could be selected with high or low. The patterning process is realized by controling the movement of the substrate through piezoelectric ceramic transducer (PZT).

Two-beam Laser Interference

Compared with LDW, TBLI is more suitable for fast, periodic and large area structures fabrication. Multi beam Laser interference lithography is an emerging technology that has the capability to produce 1D, 2D and 3D structures on a variety of substrates. SERS substrates also benefit from the large area periodic structures. So in this thesis, TBLI patterning was also applied for the template fabrication. In this section, I will introduce TBLI technique both on its basic principle, experimental setup and simulation result.

In the Young's double slit experiment, the coherent light from two slits was allowed to interact to form the interference fringes. To achieve the coherent light is one key issue for this interference process. As the development of Laser technique, viarious types of lasers are available which can produce single frequency light, for example, monochromatic light. The monochromatic light can be splitted into two beams of coherent light by optical components. If these two coherent ligh was ajusted illuminating on a same spot, they will overlap and produce the superposition of two light waves. Such a superposition of light will produce bright and dark fringes (so-called interference patterns) on the substrate similar to that of Young's double slit experiment. The bright stripes and the dark stripes are formed at the places where two light waves interfere constructively and destructive interference produces respectively, as shown in Figure 1.2. A diffraction gratings pattern is formed consisting of alternate grooves due to the intensity distribution and phase relation of the two beams.

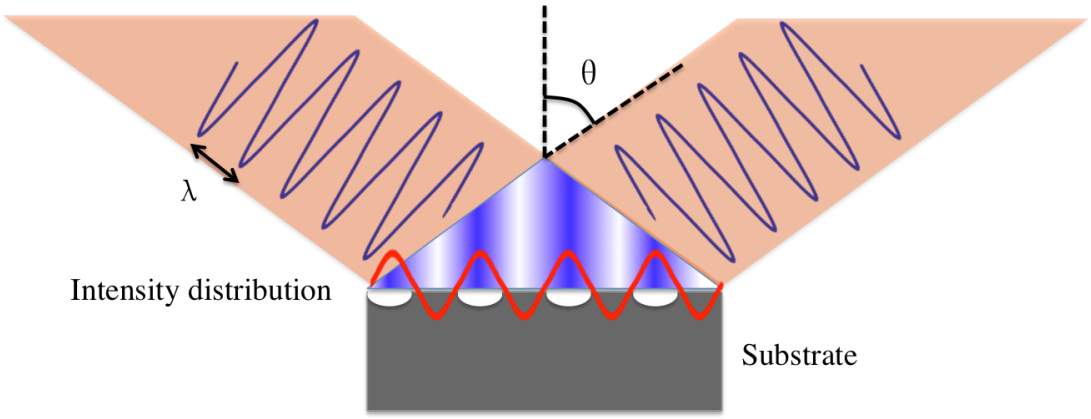

Figure 1.2 Scheme of TBLI fabrication process.

The intensity I_x along the substrate surface in plane, at any location of the interference pattern is given by

$$I_x = I_1 + I_2 + 2\sqrt{I_1 I_2} \times \cos\varphi\theta \tag{1.9}$$

Where, I_1 and I_2 are the intensities of the two beams. And φ is the phase difference between the two beams, which is produced by the angle θ and distance mismatch between them. If the two beams are symmetric without distortion, periodic diffraction gratings can be formed, which was well known as Bragg gratings. The periodicity L of this grating pattern is described by

$$L = \frac{\lambda}{2\sin\theta} \tag{1.10}$$

Here, λ is the wavelength of the laser, which is hard to change in practical operation. Thus the period of the gratings can be tuned by adjusting the angle between the two laser beams.

There are mainly two types of configurations to generate the interference patterns, which are so called: Wavefront Splitting Interferometers (WSI) and Amplitude Splitting Interferometers (ASI).

WSI: this configuration is relatively simple and benefits from better stability and easy controllability. It is usually utilized for high-resolution inference patterning. In details, there are many different classical methods to realize WSI. Such as:

i). Using specially designed prisms to divide a single laser beam into a number of beams, followed by superposition them onto a same square [29, 30]. This method is especially helpful for multi-beam interference pattern [31]. Normally, to get a defect free and symmetric interference pattern, the prism refractive index should match that of the substrate material.

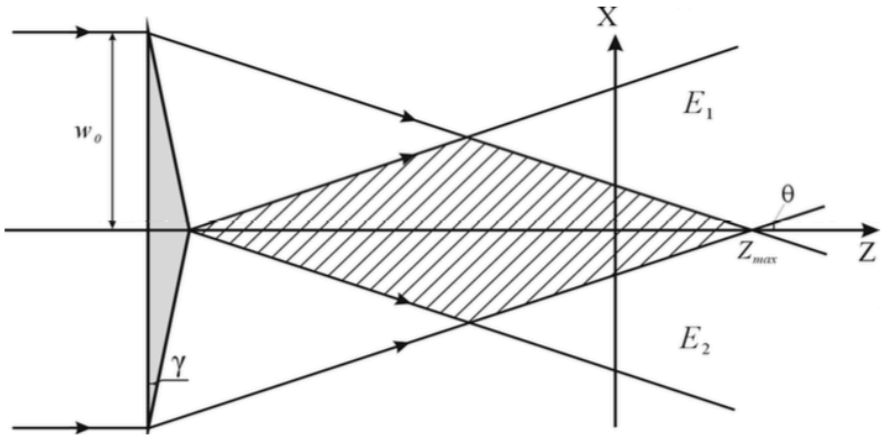

Figure 1.3 Plane geometrical scheme of WBI configuration using a symmetric glass pyramid prism [30].

Figure 1.3 shows an example of two beams WSI system, an expanded laser beam passes through a symmetric glass pyramid, then divided into two sub-beams due to refraction. Each beam is inclined by an angle θ with respect to the optical axis. The resulting interference zone (shadow region) covers from 0 to $Z_{max} \approx W_0/tan\theta$, where W_0 is half of the beam width. Usually a very small angle θ is preferable to have a sufficiently extended interference zone.

ii). Applying diffraction gratings to cause the interference. A single beam source is first divided by one or two diffraction gratings. The first order-diffracted beams are then directed to interfere on the substrate surface [32-34]. Figure 1.4 illustrates the detail processes, the glass substrate contains gratings structure on both upper and bottom sides. Passing through the gratings structures, the coherent light will form two first-order and two second-order diffracted beams. These two second-order beams will interfere and form interference patterns on the sample when placed with a proper distance away from the center.

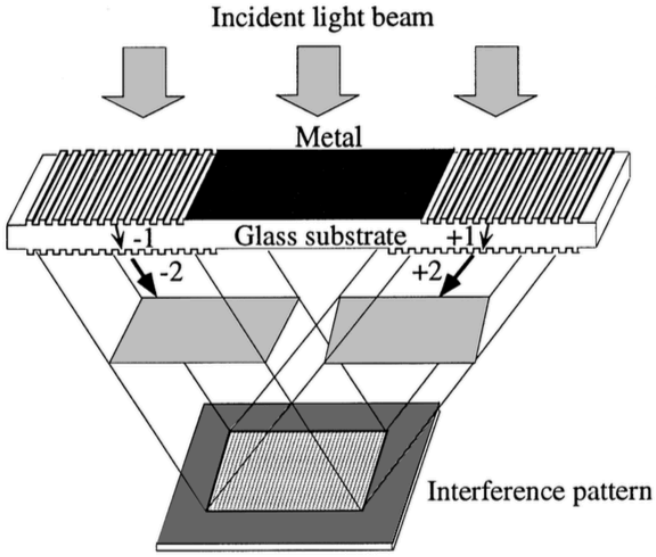

Figure 1.4 Schematic diagram for WSI configuration by applying diffractive gratings [33].

iii). Lloyd's mirror interferometer, which is known as the most commonly used wavefront splitting configuration, is illustrated in Figure 1.5. In this method a single expanded laser beam is used, and one part of it is reflected by a mirror and interfered with the other portion of the beam. The reflection mirror and substrate are mounted on a rotatable stage, by which the angle θ between normal plane to the substrate surface and the incident light can be adjusted. The period of this grating pattern is determined by the equation 1.10, thus by controlling the stage rotation the period of the grating pattern can be easily tuned.

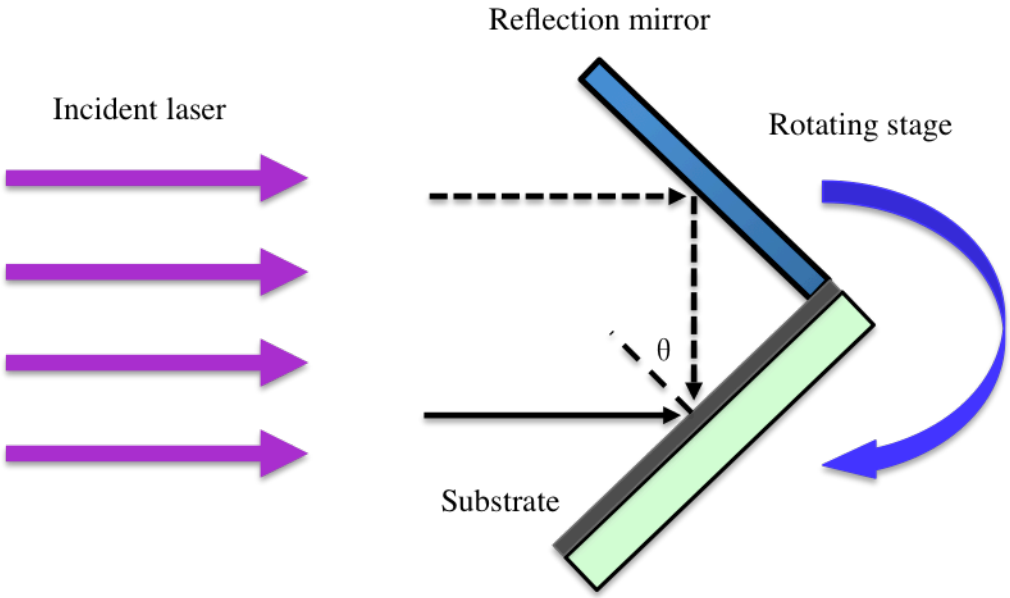

Figure 1.5 Scheme of Lloyd's mirror interferometer. The Bragg grating pattern is achieved by the superposition of the light reflected from the mirror surface (upper dotted line) and the part of light directly illuminating the surface of substrate (lower solid line).

In Lloyd's mirror configuration, to get satisfied patterning performance, usually the setup is placed on a vibration free table to avoid the vibration of the system elements and limit the differences in the optical path. Also the quality of the mirror surface is another key issue for achieving a perfect interference pattern. Recently, various modified configurations of Lloyd's mirror method have been employed to fabricate 2D and 3D structures [35, 36].

ASI: compared with WSI, ASI configurations are usually applied for large area patterning. Choosing Dual Beam Interferometer as an example, as shown in Figure 1.6, a single laser beam is expanded (to increase the interference area) by L1 and collimated by L2 before being divided into two beams by a beam splitter. Then all the resulting secondary beams are directed by adjusting reflection mirrors M1 and M2. As the intensities of the two beams are same and optical paths distances are also equal, when they overlap on the substrate surface, a periodic interference pattern can be obtained. The period of the pattern is also determined by Equation 1.10, which can be tuned by changing the angle θ between the laser and the normal direction of the substrate. If one wants to make complex 2D or 3D structures, exposure of multi-beams [37-39] or multi-steps exposures of two beams can be used [40-42].

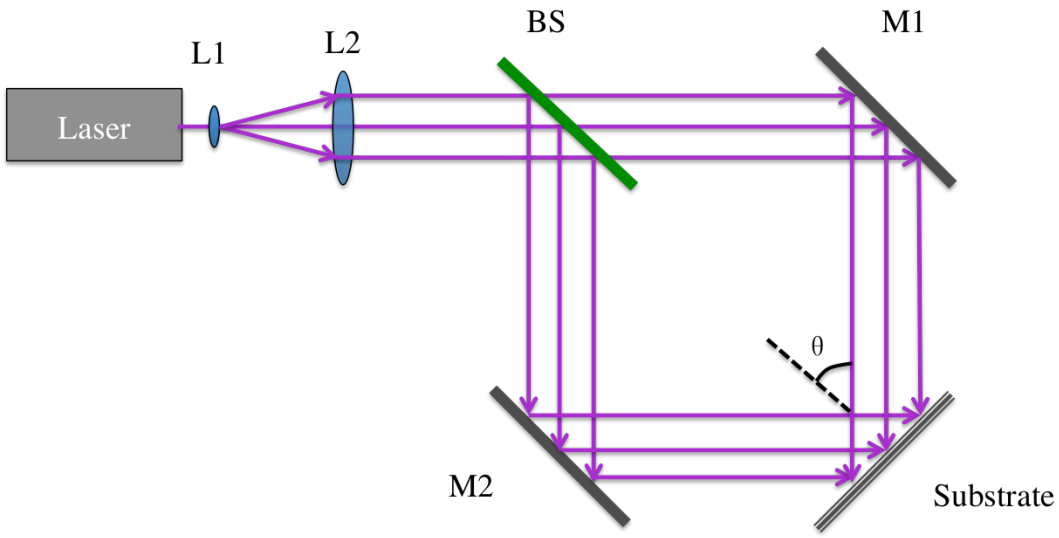

Figure 1.6 Schematic of the two-beam ASI configuration.

In order to achieve a uniform pattern without defects and fluctuations, the ASI setup should be free from airflows and vibrations. In this thesis, ASI method was utilized to pattern grating patterns as the template for SERS substrate fabrication, it will be discussed in next chapter in detail.

1.3 FIB-structured surface

Focused ion beam (FIB) technique has attracted more and more researchers' interest since it was first introduced by Seliger and Fleming for maskless ion implantation into Si in 1974 [43]. For FIB has many remarkable advantages for nanostructures fabrication and maskless processes [44, 45], such as: scanning ion microscopy (SIM), maskless etching and deposition, maskless doping. It becomes a powerful technology in structured surface science world.

Fundamentals of FIB

The configuration of FIB system is illustrated in Figure 1.7. It contains ion source (usually Ga), ion extractor, ion beam modulation elements, secondary electron detector MCP. Its working process is as follows: the ions first are extracted by strong electric field, and then purified by $E \times B$ mass analyzer and neutral beam shifter, accelerated and finally focused on sample surface, through the deflection and scanning elements, desired structures could be patterned.

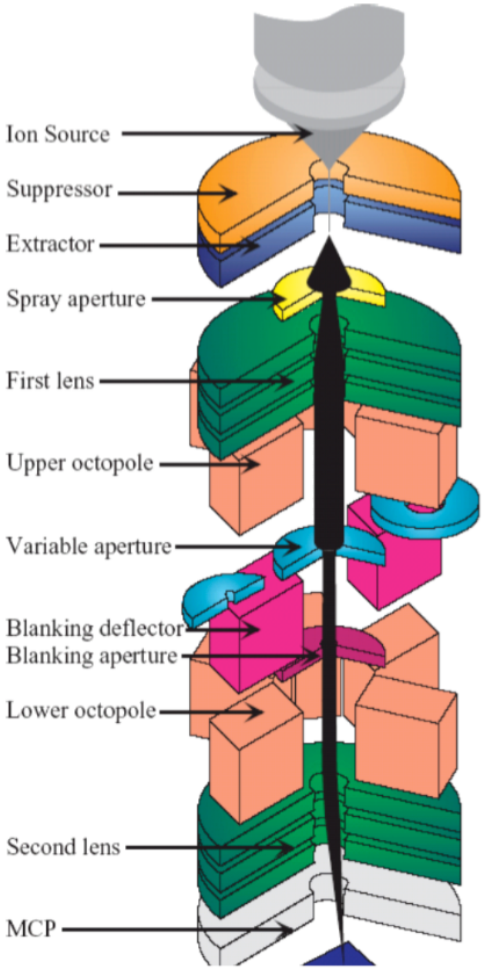

Figure 1.7 Scheme of FIB

The interaction between high-energy ions and substrate materials is illustrated in Figure 1.8. High speed ions hit the sample surface and sputter a small amount of material, including secondary ions (i^+ or i^-), neutral atoms (n_0) and secondary electrons (e^-). The primary ions collide with the lattice atom and electron, gradually loose energy and finally stop in the substrate, this process is called ion implantation. The implantation depth R_p is proportional to the ions acceleration energy. Together with implant dopants, plenty of lattice disorder will also be introduced during ions implantation process.

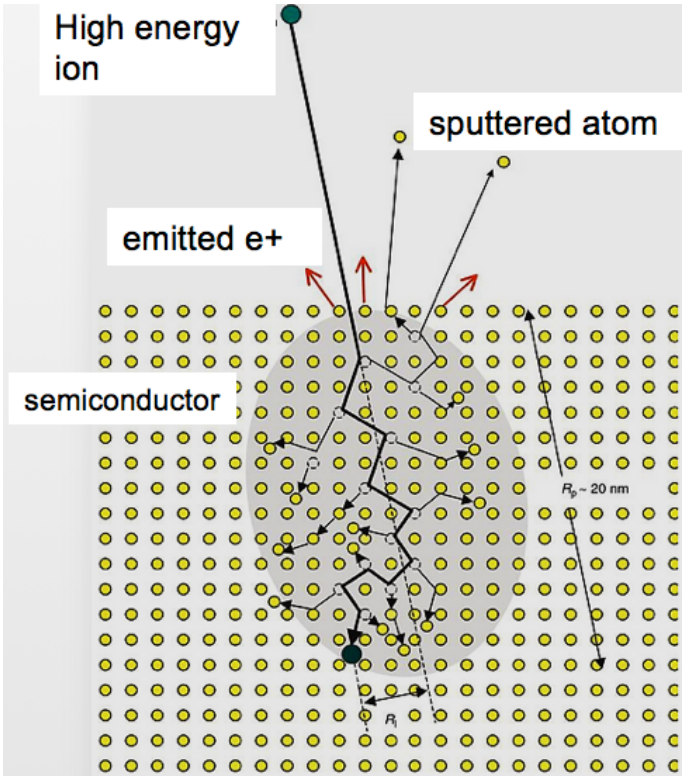

Figure 1.8 Scheme of interaction of focused ions with substrate

FIB for doping

FIB has been widely used for imaging, etching and deposition with nanometer resolution [46-47]. Actually, besides these applications, FIB is also powerful for nanoscale doping, compared with normal ion implantation or lithography methods, it has the advantages of mask-free and flexible for desired pattern.

In order to make good doping process, we should pay more attention to several parameters, such as: ions voltage, current, dose, ions injecting angle with respect to the sample surface. The ions voltage determines the doping depth and surface damage. Normally in case of ions voltage V_{ion}<40kV, the doping depth R_p is proportional to the voltage as: $R_p \propto V_{ion}$, example for 20kV ions, the doping depth is about 20nm. It means the doped ions are distributed in the 20nm thick surface layer. Also, the surface damage also related to the ions voltage, for large voltage the surface damage will be bad. The dose of the dopant is calculated by: $N = \frac{I_{ion} \cdot t}{S \cdot e}$, Here I_{ion} is the ions current, t is the doping time, e is the electron charge value and S is the doped area. So by choosing a proper ion current and doping time, it is convenient to tune the dose on the surface. Here we should also notice the crystal surface direction to avoid the channel effect during doping, it will greatly affect the doping depth and dose.

Summary

In this chapter, I first introduced the basic knowledge of structured surface, including its development and challenges. In order to solve these challenges, laser patterning method and FIB were proposed for making effective structured surface. To get readers a well understanding on these two technologies, they are in detail illustrated, such as their fabrication mechanisms, setup configurations and operation specifics.

References:

[1]. T. Vitu, T. Polcar, L. Cvrcek, R. Novak, J. Macak, J. Vyskocil *et al.*, *Surface and Coatings Technology* **202**, 5790-5793 (2008).

[2]. M. Congreve, C. W. Murray, T. L. Blundell, *Drug discovery today* **10**, 895-907 (2005).

[3]. Y. Matsuura, M. Kusunoki, W. Harada, M. Kakudo, *Journal of Biochemistry* **95**, 697-702 (1984).

[4]. A. Królikowska, A. Kudelski, A. Michota, J. Bukowska, *Surface science* **532**, 227-232 (2003).

[5]. I. Etsion, *Journal of tribology* **127**, 248-253 (2005).

[6]. S. Matsui, Y. Ochiai, *Nanotechnology* **7**, 247 (1996).

[7]. P. Nordlander, F. Le, *Applied Physics B* **84**, 35-41 (2006).

[8]. A. V. Pinheiro, D. Han, W. M. Shih, H. Yan, *Nature nanotechnology* **6**, 763-772 (2011).

[9]. B. Sharma, R. R. Frontiera, A.-I. Henry, E. Ringe, R. P. Van Duyne, *Materials today* **15**, 16-25 (2012).

[10]. D. Cialla, A. März, R. Böhme, F. Theil, K. Weber, M. Schmitt *et al.*, *Analytical and bioanalytical chemistry* **403**, 27-54 (2012).

[11]. Z. Cui, *Micro-nanofabrication: technologies and applications*. (Springer, 2006).

[12]. C. A. Jackson, P. Buck, S. Cohen, V. Garg, C. Howard, R. M. Kiefer *et al.*, *Proc Spie* **5377**, 1005-1016 (2004).

[13]. X. Wu, *Materials Science & technology* **23**, 631-640 (2007).

[14]. S. Kawata, H. B. Sun, T. Tanaka, K. Takada, . *Nature* **412**, 697-698 (2001).

[15]. X. Hong, W. Juan, T. Ye, C. Qi-Dai, D. Xiao-Bo, Z. Yong-Lai *et al.*, *Advanced Materials* **22**, 3204-3207 (2010).

[16]. J. Wang, Y. He, H. Xia, L. G. Niu, R. Zhang, Q. D. Chen *et al.*, *Lab on A Chip* **10**, 1993-1996 (2010).

[17]. W. Juan, X. Hong, X. Bin-Bin, N. Li-Gang, W. Dong, C. Qi-Dai *et al.*, *Optics Letters* **34**, 581-583 (2009).

[18]. Kumar, A. Gupta, R. Kant, A. S. Nadeem, N. Tiwari, J. Ramkumar *et al.*, *Journal of Micro/Nanolithography, MEMS, and MOEMS* **13**, 019801-019801 (2014).

[19]. Yao-Yu, T. Nobuyuki, T. Takuo, D. Xuan-Ming, K. Satoshi, *Small* **5**, 1144-1148 (2009).

[20]. B. Xu, H. Xia, L. G. Niu, Y. L. Zhang, K. Sun, Q. D. Chen *et al.*, *Small* **6**, 1762-1766 (2010).

[21]. P. P. Pronko, S. K. Dutta, D. Du, R. K. Singh, *Journal of Applied Physics* **78**, 6233 6240 (1995).

[22]. B. N. Chichkov, C. Momma, S. Nolte, F. Von Alvensleben, A. Tünnermann, *Applied Physics A* **63**, 109-115 (1996).

[23]. S. Anisimov, B. Kapeliovich, T. Perelman, *Zh. Eksp. Teor. Fiz* **66**, 375-377 (1974).

[24]. M. Agranat, S. Anisimov, S. Ashitkov, B. Makshantsev, I. Ovchinnikova, *Sov. Phys. Solid State* **29**, 1875-1881 (1987).

[25]. P. Corkum, F. Brunel, N. Sherman, T. Srinivasan-Rao, *Physical review letters* **61**, 2886 (1988).

[26]. P. B. Allen, *Physical review letters* **59**, 1460 (1987).

[27]. S. Brorson, A. Kazeroonian, J. Moodera, D. Face, T. Cheng, E. Ippen *et al.*, *Physical Review Letters* **64**, 2172 (1990).

[28]. X. Wang, D. M. Riffe, Y.-S. Lee, M. Downer, *Physical Review B* **50**, 8016 (1994).

[29]. Xiang W., Liang J., Zhang G., et al., Chin. Opt. Lett. **3**, 712-714 (2005).

[30]. N. H. Rizvi, M. C. Gower, *Applied Physics Letters* **67**, 739-741 (1995).

[31]. L. Ming, Y. Baoli, R. Romano A, *Optics Express* **14**, 5803-5811 (2006).

[32]. V. Berger, O. Gauthier-Lafaye, E. Costard, *Journal of Applied Physics* **82**, 60-64 (1997).

[33]. C. H. Lin, Z. H. Zhu, Y. H. Lo, *Applied Physics Letters* **67**, 3072-3074 (1995).

[34]. H. H. Solak, *Microelectronic Engineering* **78**, 410–416 (2005).

[35]. Y. Guan, A. J. Pedraza, *Mrs Proceedings* **818**, 335-340 (2004).

[36]. D. B. Johannes, G. Nadine, G. S. Ulrich, S. Volker, *Optics Letters* **34**, 1783-1785 (2009).

[37]. Rodriguez, M. Echeverría, M. Ellman, N. Perez, Y. K. Verevkin, C. S. Peng *et al.*, *Microelectronic Engineering* **86**, 937–940 (2009).

[38]. Y. Shu, M. Megens, J. Aizenberg, P. Wiltzius, P. M. Chaikin, W. B. Russel, *Chemistry of Materials* **14**, 2831-2831 (2002).

[39]. T. Kondo, S. Matsuo, S. Juodkazis, V. Mizeikis, H. Misawa, *Applied Physics Letters* **82**, 2758-2760 (2003).

[40]. M. Miyake, Y. Chen, #x, Chieh, P. V. Braun, P. Wiltzius, *Advanced Materials* **21**, 3012–3015 (2009).

[41]. R. C. Gauthier, K. W. Mnaymneh, *Optics & Laser Technology* **36**, 625–633 (2004).

[42]. F. Y. Lee, K. H. Fung, T. L. Tang, W. Y. Tam, C. T. Chan, *Current Applied Physics* **9**, 820–825 (2009).

[43]. R. Seliger, W. Fleming, *Journal of Applied Physics* **45**, 1416-1422 (1974).

[44]. V. Wang, J. Ward, R. Seliger, *Journal of Vacuum Science & Technology* **19**, 1158-1163 (1981).

[45]. R. Seliger, R. Kubena, R. Olney, J. Ward, V. Wang, *Journal of Vacuum Science & Technology* **16**, 1610-1612 (1979).

[46]. S. Reyntjens, R. Puers, *Journal of Micromechanics and Microengineering* **11**, 287 (2001).

[47]. L. A. Giannuzzi, *Introduction to focused ion beams: instrumentation, theory, techniques and practice*. (Springer Science & Business Media, 2006).

Chapter 2.

Raman characterization on structured surface

Raman spectroscopy is usually considered as a powerful complementary method of infrared (IR) absorbance spectroscopy to characterize molecules' composition or structures [1]. Raman spectroscopy could provide molecular and structure information which is usually not available by IR absorbance spectroscopy or fluorescence. It has great potential usage on structured surface to evaluate its plasmonic properties and identify structure changes. In this chapter, Raman spectroscopy is introduced from fundamentals to performance on characterizing laser-structured plasmonic surfaces and FIB-structured semiconductor surface.

2.1 Fundamentals of Raman spectroscopy

Raman scattering was first found in a liquid sample and reported by C. V. Raman and K. S. Krishnan in 1928 [2], and then named this effect by the name of Raman. In the same year G. Landsberg and L. I. Mandelstam also reported similar phenomena in crystals [3]. Actually before C. V. Raman, Adolf Smekal had already theoretically predicted this effect earlier in 1923 [4]. Raman spectroscopy is usually used in the area of chemistry and biology, for it can provide rich information of molecules by observing their structural vibrational, rotational and other low frequency modes [5, 6].

Principle of Raman scattering

When light illuminates on subjects, scattering process usually happens together with absorptions. This process could also be considered as the interaction between photons and molecules. Most of the scattered light just changes the propagation direction without changing the frequency, this process is called Rayleigh scattering, also known as elastic scattering for no energy transfer (between photons and electrons) happens during this process [7]. While small part of the scattered light changes not only the propagation direction but also the frequency, for the incident photons' energy is either gained or lost during the collision with the molecules. This inelastic scattering is called Raman scattering [2]. Figure 2.1 shows the schematic illustration of Rayleigh scattering and Raman scattering.

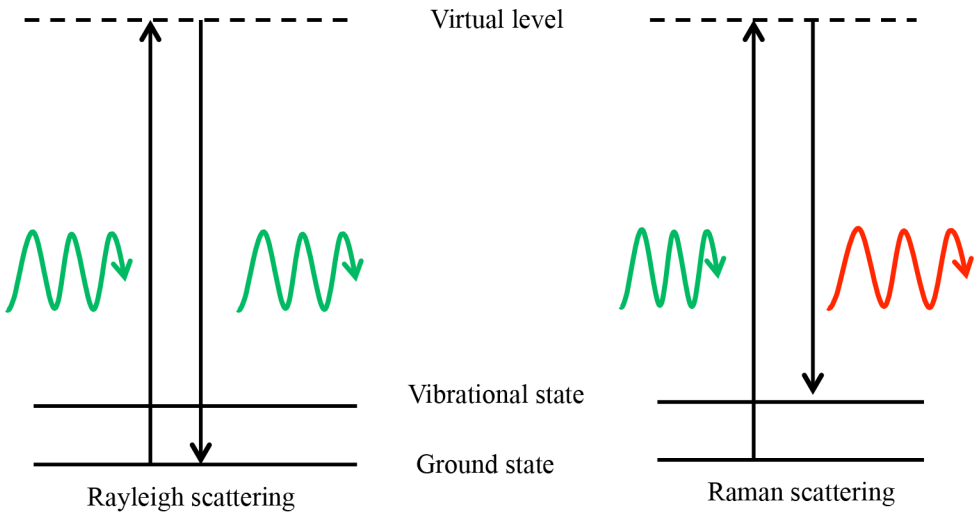

Figure 2.1 Scheme of Rayleigh (left) and Raman (right) scattering.

When incident light illuminates a subject and interacts with the intermolecular electronic system, the outer-shell electrons first absorb the incident photons and go up from the ground energy state to a higher virtual level (not high enough to reach an excited level). For the virtual level is not stable, the electrons will soon go back to the ground state and release the absorbed photons; or go back to a vibrational state and emit energy-shifted photons, as shown in the left and right Figure in Figure 2.1 respectively.

Theoretically, light is one kind of electromagnetic wave, it can be expressed as equation 2.1:

$$\mathbf{E} = \mathbf{E}_0 \cos 2\pi\upsilon t \tag{2.1}$$

In the equation, **E** is the electric field of the light with frequency υ and amplitude $\mathbf{E_0}$. When illuminated with light, the molecules interact with the electromagnetic wave and would be polarized and generate a dipole, the dipole moment $\boldsymbol{\mu}$ could be expressed as below:

$$\boldsymbol{\mu} = \boldsymbol{\alpha}\mathbf{E} = \boldsymbol{\alpha}_0\mathbf{E}_0 \cos 2\pi\upsilon \mathrm{t} \tag{1.2}$$

Where $\boldsymbol{\alpha}$ is the polarizability tensor of the molecule. It can be defined as

$$\boldsymbol{\alpha} = \boldsymbol{\alpha}_0 + \boldsymbol{\beta}\cos 2\pi\upsilon_R \mathrm{t} \tag{2.3}$$

Where $\boldsymbol{\alpha}_0$ is static or equilibrium polarizability tensor, $\boldsymbol{\beta}$ is the vibrational modulation of molecular polarizability tensor at molecular vibration frequency υ_R. Then equation 2.2 could be further written as

$$\boldsymbol{\mu} = \boldsymbol{\alpha}\mathbf{E} \quad = \boldsymbol{\alpha}_0\mathbf{E}_0 \cos 2\pi\upsilon \mathrm{t} + \mathbf{E}_0\boldsymbol{\beta}\cos 2\pi\upsilon t \cos 2\pi\upsilon_k t$$

$$= \boldsymbol{\alpha}_0\mathbf{E}_0 \cos 2\pi\upsilon \mathrm{t} + \frac{1}{2}\mathbf{E}_0\boldsymbol{\beta}\left[\cos 2\pi\left(\upsilon + \upsilon_k\right)t + \cos 2\pi(\upsilon - \upsilon_k)t\right] \tag{2.4}$$

From equation 2.4, it is very easy to get the point that, during the scattering process, there are energy transfer between the incident photons and the molecular vibration modes (so called phonons). Thus the scattered light contains some frequency-shifted part, as shown in the later expression in equation 2.4, which could be detected and processed as Raman shift signal υ_R. The unchanged frequency ν responds to Rayleigh scattering as shown in the center ribbon in Figure 2.2. While the frequency-downshifted $(\nu - \nu_R)$ and frequency-upshifted part $(\nu + \nu_R)$ represents the Stokes and anti-Stokes scattering respectively, as shown in the two sides part in Figure 2.2.

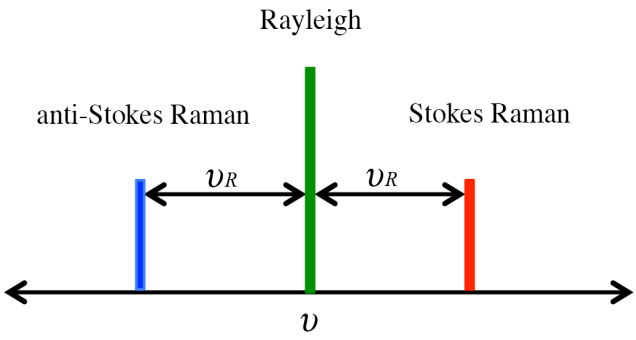

Figure 2.2 Schematic illustration of Rayleigh, Stokes Raman and anti-Stokes Raman scattering spectra.

As the Raman shift modes represent the molecule's vibration modes, which directly related to the molecule's composition and structure. By observing analyzing the Raman shifts, researchers could know the details of molecule's information and then even manipulate the molecules' properties by external forces [8, 8]. Here we choose the Raman spectra of single-wall carbon nanotubes (SWNTs) as an example, as shown in Figure 2.3 [10, 11], there are four strong Raman bands called radial breathing mode (RBM), D band, G^+ and G^-band.

As a consensus, the SWNT columnar shape generates RBM, where each carbon atom vibrates along the radial direction. The SWNT (n, m) indices could be obtained under the resonance condition, for the RBM frequency is inversely proportional to the SWNT

diameter, [12]. In the first-order Raman spectra, the G band is considered as up to 6 C-C vibration peaks. As shown in Figure 2.3 (b), the vibrations are tangential with respect to the surface of the tube, 3 are along the tube axis (G^+ band) with the others are along the tube circumference (G^- band). G band directly related to the atom arrangement of the SWNTs, thus it could be used to evaluate the molecule quality. This of great importance by using Raman to determine the Fermi energy position [13-15]. For disorder-induced D band, it appears at ~1350cm^{-1}. The D to G intensity ratio could well indicate the size of in-plane crystallite and the amount of the sample disorder [16, 17].

From the above discussion, we know that each Raman mode contains special meaning of a molecule. However not all the vibration modes of the molecules could generate Raman modes, they follow the so-called selection rules, which means only those Raman active vibrations could be detected. In next section, I will briefly introduce the selection rules of the Raman scattering.

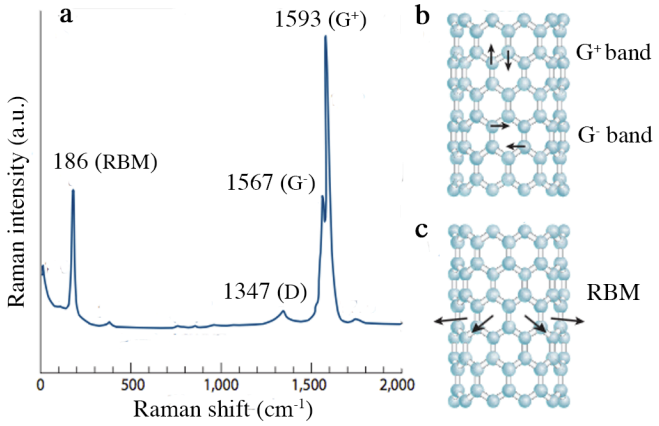

Figure 2.3 (a) Raman spectrum of a SWNT bundle. **(b)** The G^+ and G^- band eigenvectors for the C-C bond-stretching mode along the tube axis (LO) and along the circumference (TO) respectively. **(c)** Scheme of the radial breathing mode (RBM around186 cm^{-1}). [18]

Selection rules of Raman scattering

As we all know that for IR absorbance spectrum, the selection rules are that:

1. Vibration must produce a change in the dipole moment of a molecule;

2. $\Delta v = \pm 1,\ \Delta E_{v \to v+1} = hv = hw$

3. Overtones: $\Delta v = \pm 2, \pm 4 \ldots$

The second and third rule means that, the absorbed energy equals to the energy difference between two vibrational states (overtones are allowed).

While for Raman scattering, it is governed by the polarizability of the electron cloud. Thus different from IR, Raman happens when the polarizability changes. Polarizability means how easy molecule could be polarized, or how easy a charge distribution, like the electron cloud of an atom or molecule, to be distorted from its normal shape by an external electric field. To get an obvious idea of the selection rules, I choose CS_2 molecule as an example, as shown in Figure 2.4. The upper vibration mode υ_1 is Raman active, for the changed electron cloud is easier to be polarized, which means polarizability is changed. While for the lower two modes υ_2 and υ_3 are IR active as they caused the molecule's dipole moment changes.

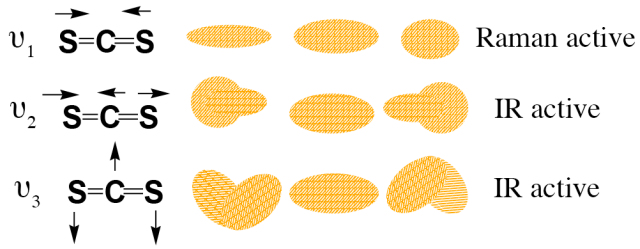

Figure 2.4 Selection rules of CS_2 molecule. $\upsilon_1, \upsilon_2, \upsilon_3$ is the symmetric stretching, asymmetric stretching and bending vibration respectively.

Theoretically, the vibration modes of molecules could be expressed as

$$Q_k = Q_{k0} \cos 2\pi \upsilon_k t \qquad (2.5)$$

Where k is the energy level number, υ_k is the vibration frequency at level k, Q_k is a normal vibrational coordinate and Q_{k0} is the maximum value Q_k. Then the derivative of the polarizability β in equation 2.3 is:

$$\beta = \frac{\partial \alpha}{\partial Q_k} Q_k \qquad (2.6)$$

The dipole μ could be written in details as

$$\mu = \alpha_0 \mathbf{E_0} \cos 2\pi \upsilon t + \frac{1}{2} \mathbf{E_0} Q_{k0} \frac{\partial \alpha}{\partial Q_k} \left[\cos 2\pi (\upsilon + \upsilon_k) t + \cos 2\pi (\upsilon - \upsilon_k) t \right] \qquad (2.7)$$

From equation 2.7, the Raman activity needs

$$\frac{\partial \alpha}{\partial Q_k} \neq 0 \qquad (2.8)$$

It means that at the equilibrium position, the derivative of the polarizability with respect to the molecular vibrations should not be zero. Actually, if consider this process with quantum theory, the condition for Raman active is

$$\int \varphi_i \mu \varphi_f d\tau \neq 0 \qquad (2.9)$$

Here φ_i and φ_f is the initial and final wave function of the system, μ is the induced dipole moment, μ could be expressed with the component form of α as

$$\mu = \begin{vmatrix} \alpha_{xx} & \alpha_{xy} & \alpha_{xz} \\ \alpha_{yx} & \alpha_{yy} & \alpha_{yz} \\ \alpha_{zx} & \alpha_{zy} & \alpha_{zz} \end{vmatrix} \begin{vmatrix} E_x \\ E_y \\ E_z \end{vmatrix} \tag{2.10}$$

Here, as molecular vibrations should be symmetric [19], the components $\alpha_{xy} = \alpha_{yx}$, $\alpha_{xz} = \alpha_{zx}$, $\alpha_{yz} = \alpha_{zy}$, so during the process of transition from i to f, there are 6 components, among which, only if one is not zero, Raman is active as equation 2.9 illustrates. So we just need to consider its symmetry. Due to group theory, φ_i is the molecular initial wave function, and then the simple harmonic wave $\varphi_\lambda = \varphi_\lambda^o e^{2\pi i(E_i/h)t}$ is totally symmetric. Thus only when α_{xy} and φ_f belong to the same type of symmetry, the transition of i to f is Raman active. The symmetric representations of a symmetric system are summarized in the so-called character table. By checking the character table, one can easily know a molecular vibration is Raman active or not.

2.2 Plasmonic enhancement

Plasmonic structures are designed to enhance the weak optical signal through generating strong localized surface plasmon polaritons (SPPs). However, it is still under development. To evaluate and improve the performance of the plasmonic properties is of great value. Compared with other methods, Raman is an advance one for evaluation the plasmonic structures. For it is non-destructive, tag free and easy sample preparation. By observing the enhanced Raman signal on the structured surface, the electromagnetic enhancement factor and the reproducibility can be clearly understood. Thus it is of great value for the improvement for the plasmonic structures design and fabrication.

Enhanced Raman on plasmonic structures

In general, the enhancement of SERS could be attributed to two mechanisms: the electromagnetic enhancement mechanism (EM) and chemical enhancement mechanisms (CM). As the former one is normally considered as the dominating mechanism for high SERS enhancement, in this thesis, I mainly talk about EM.

The EM is also called physical enhancement mechanism, which involved so-called localized surface plasmon polaritons (LSPPs). Plasmon can be physically considered as a quasi-particle, which arises from the quantization of plasma oscillations, just as that phonons are quantized mechanical vibrations. Plasmon can couple with photon to create another quasi-particle called plasmon polaritons. However, plasmon can only couple with photon on the surface of a bulk metal. The reason is shown in Figure 2.5.

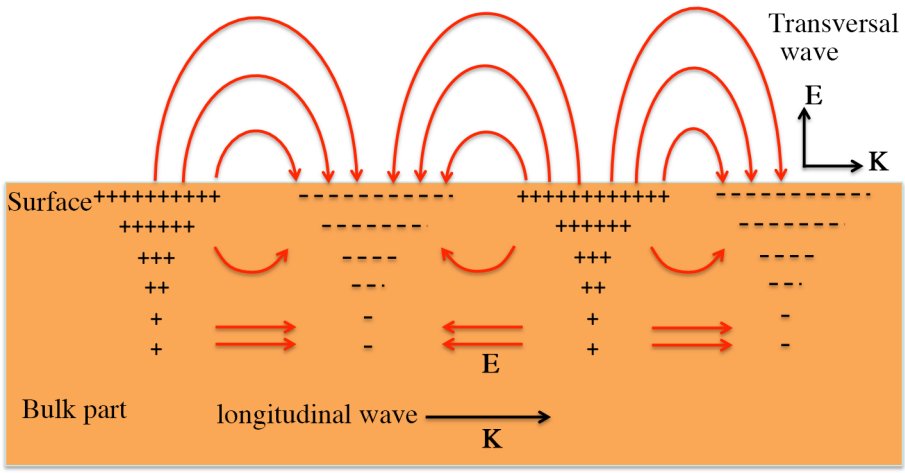

Figure 2.5 Plasmons propagating on the surface and in the bulk of a metal material. Especially on the surface, plasmon contains transversal wave components that can couple with phonon.

Plasmon is longitudinal wave, while photon is transversal wave, in the bulk part of a metal, they won't couple; on the surface (interface between the metal and other dielectric substance), there appear transversal wave components, which could couple with the incident photons, to form surface plasmon polaritons (SPPs).

For SPPs on a perfectly flat surface are always nonradiative. They could not enhance the electromagnetic filed even possess large condensed energy. To make SPPs be radiative, metal NPs with size smaller than light wavelength are usually used. So when a light wave interacts with metal NPs, LSPPs could be consequently induced in the vicinity of the NPs, by means of free electrons collectively oscillating, as shown in Figure 2.6. The positions that have the enhanced localized electric field are also named hotspots. Thus when molecules approach to these hotspots, their Raman scattering signals can be dramatically amplified.

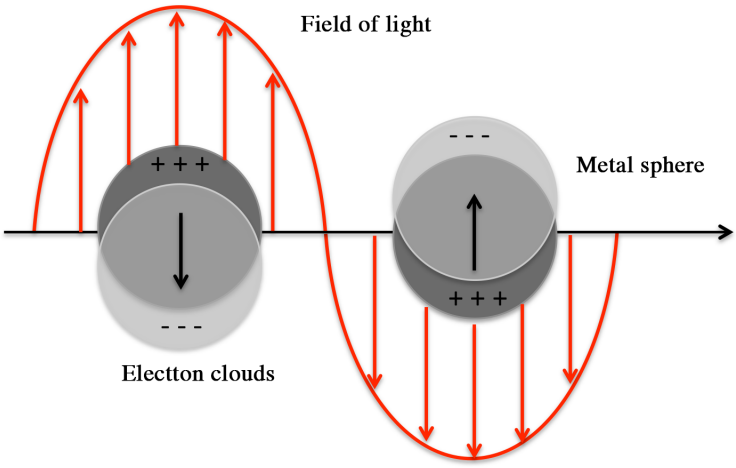

Figure 2.6 Illustration of the localized plasmon polaritons near metal surfaces induced by electromagnetic field of incident light.

As the size of the metal nanoparticle is relatively small than the incident wavelength, to simplify the situation, quasi-electrostatic approximation can be applied to analyze this system. In quasi-electrostatic approximation, the phase retardation is neglected due to theory of the LSPPs [20, 21]. From Mie scattering equation, the induced LSPP can be

treated as a dipole centers at the metal nanoparticle under an external electric field. The dipole moment μ can be illustrated as

$$\mu = \varepsilon_1 \alpha_m E_0 \tag{2.11}$$

In here, ε_1 is the relative permittivity of the surrounding material, E_0 is the electric field of the incident light, and α_m is the polarizability of the metal nanoparticle, which can be expresses as：

$$\alpha_m = 4\pi r^3 \frac{\varepsilon_m(\omega_i) - \varepsilon_1}{\varepsilon_m(\omega_i) + 2\varepsilon_1} \tag{2.12}$$

Where r is the radium of the metal nanoparticle ($r \ll \lambda$), and $\varepsilon_m(\omega_i)$ is the complex permittivity of the metal at angular frequency ω_i. From equation 2.11 and equation 2.12, the amplitude of the dipole moment μ will drastically increase, when the resonance of the LSPPs happens. In this case, $\mathrm{Re}(\varepsilon_m) + 2\varepsilon_1 = 0$ is satisfied, where $\mathrm{Re}(\varepsilon_m)$ is the real part of ε_m and becomes negative ($\mathrm{Re}(\varepsilon_m) = -2\varepsilon_1$).

As the strongly induced dipole moment could also greatly enhance the electric field in the vicinity of the metal NPs. The maximum value of the enhanced local electric field E_{loc} is described as equation 2.13.

$$E_{loc} = 2\frac{\varepsilon_m(\omega_i) - \varepsilon_1}{\varepsilon_m(\omega_i) + 2\varepsilon_1} E_0 \tag{2.13}$$

Hence the enhancement of the local E-field intensity M_{loc} under LSPPs resonance condition can be written as

$$M_{loc} = \left| \frac{E_{loc} + E_0}{E_0} \right|^2 \tag{2.14}$$

Introducing equation 2.13 into equation 2.14, and assuming the permittivity of the metal in a form as $\varepsilon_m(\omega_i) = \varepsilon'_m(\omega_i) + i\varepsilon''_m(\omega_i)$, one finds

$$M_{loc} = \left| \frac{3\varepsilon_m(\omega_i)}{\varepsilon_m(\omega_i) + 2\varepsilon_1} \right|^2 = 9\left\{ \left[\frac{\varepsilon'_m(\omega_i)}{\varepsilon''_m(\omega_i)} \right]^2 + 1 \right\} \tag{2.15}$$

To get a higher enhancement, the smaller imaginary part of the permittivity $\varepsilon''_m(\omega_i)$ is the better. That is why silver and gold are usually selected as the material for SPPs generation in the visible light range.

When Raman scattering was enhanced by such LSPPs, the scattered Raman field would also be enhanced by a factor M_s similar as M_{loc}, for the frequency of the scattered Raman signal is not so much different from the incident light frequency: $\omega_s \approx \omega_i$. Thus the total Raman enhancement factor EF can be described as

$$EF = M_{loc} M_s \approx M_{loc}^2 \approx \left| \frac{E_{loc}}{E_0} \right|^4 \approx 81 \left[\frac{\varepsilon'_m(\omega_i)}{\varepsilon''_m(\omega_i)} \right]^4 \tag{2.16}$$

Obviously, to get a high enhancement factor for a SERS measurement, enhancing the localized E-field is the most effective way. For example, if the LSPPs enhanced the

localized E-field by 10 times, the Raman signals of molecules can be increased by 10000 times. In fact, by choosing a proper material (e.g. with a high $\varepsilon'_m(\omega_i)/\varepsilon''_m(\omega_i)$), optimizing the size, and junction features of plasmonic nanostructures, a SERS EF can reach or be even larger than 10^{10} [22]. Consequently, the cross section of SERS can be established by multiplying the Raman cross section with the EF of SERS, which will reach about 10^{-20}. This value supports SERS being applied in various areas with its powerful analyzing potential. Then the key issue becomes how to design and fabricate effective structures as SERS substrates.

On well understanding the mechanisms of SERS, by Raman study on the metallic structured surface, we know that both the frequency and magnitude of the maximum enhanced E-field strongly depend on the proper materials, sizes, shape and arrangement of the metallic nanostructures. These information is important for designing effective plasmonic structures for the application as chemical and biological sensors.

2.3 High resolution Raman imaging

From Raman spectra, one can know the molecular or crystal spices and structure information, which is usually called fingerprint of a sample. By taking Raman image of a sample, it will give us more useful information, such as the distribution of the target molecule, lattice structures and chemical bonds [23]. This is of great value on analyzing the dynamic process in physics, chemistry and biology.

Raman imaging on doped semiconductor surface

In ICs industry, the doping process plays a key role for reforming the surface electronic properties. Usually the doping property is hard to characterize by the traditional methods (AFM, SPM), as there is less surface morphology change on the doped

structures. While Raman showed its features on characterizing crystal lattice changes here.

Figure 2.7 schematically illustrates the crystal lattice changes and Raman responses in the doped area. From a Raman spectrum of a perfect semiconductor, we can find several characteristic Raman peaks which relate to the special phonon modes of the crystal. When doped with some different ions, the Raman spectrum of the doped area will show some additional modes or Raman peak position shifts that related to the new doped atoms, such as lattice disorder or localized strain forces [24]. Thus when imaging at these abnormal modes, the doped area can be clearly observed; the localized composition and structure property can also be analyzed. This will help understanding the crystal changes during doping process, and improve the doping techniques in IC industry.

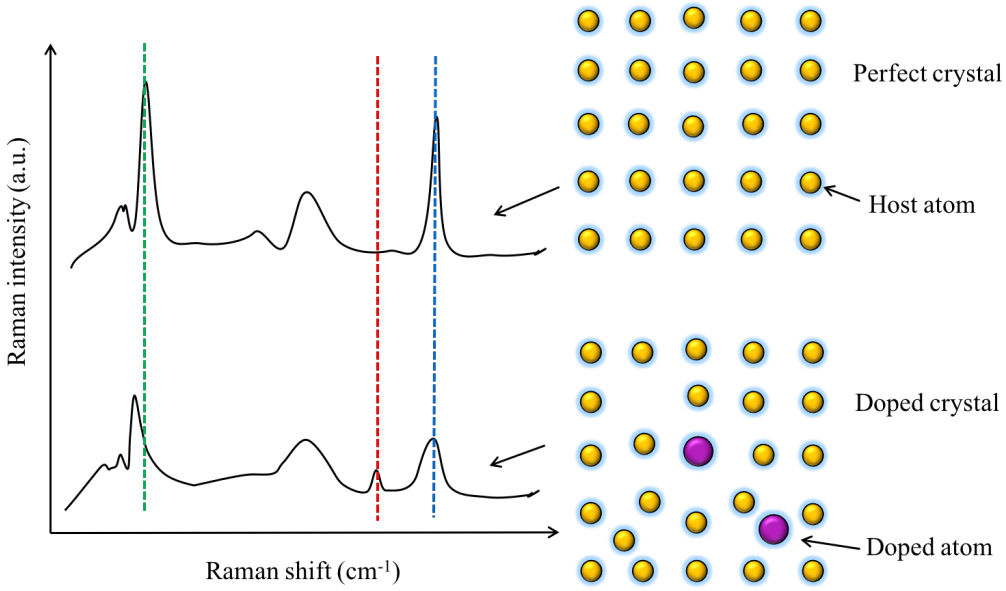

Figure 2.7 Scheme comparison of Raman spectra from perfect crystal and doped crystal (left). Scheme of crystal structures of perfect crystal and doped crystal (right).

Summary

In this chapter, I first introduced the basic knowledge of Raman spectroscopy, including its principle, selection rules, and its applications in various areas. Then I talked about enhanced Raman on plasmonic structures, the principle of SERS enhancement, which is strongly dependent on the localize-enhanced electric field on plasmonic surfaces. The SERS enhancement can be greatly increased by choosing proper material, optimized size, shape and arrangement of the metal nanoparticles. Finally, I talked about high resolution Raman imaging on ion doped semiconductor surface, which can characterize the crystal structure changes and their special distributions. It is of great value to understand the doping process and improve IC technologies.

References:

[1]. L. C. Prinsloo, A. Tournie, eacute, P. Colomban, *et al.*, *Journal of Archaeological Science* **40**, 2981–2990 (2013).

[2]. C. V. Raman, K. S. Krishnan, *Nature* **121**, 501-502 (1928).

[3]. L. M. Surhone, M. T. Tennoe, S. F. Henssonow, R. Scattering, R. Law, J. Strutt *et al.*, *Rayleigh Scattering*. (Betascript Publishing, 2010).

[4]. A. Smekal, *Naturwissenschaften*, **11**(43), 873–875, (1923).

[5]. D. Cialla, A. März, R. Böhme, F. Theil, K. Weber, M. Schmitt et al., *Analytical and bioanalytical chemistry* **403**, 27-54 (2012).

[6]. M. E. Stewart, C. R. Anderton, L. B. Thompson, J. Maria, S. K. Gray, J. A. Rogers *et al.*, *Chemical reviews* **108**, 494-521 (2008).

[7]. Surhone, L. M., Tennoe, M. T., Henssonow, S. F., Scattering, R., Law, R., & Strutt, J., et al., Rayleigh Scattering. *Betascript Publishing*, (2010).

[8]. T. Yano, T. Ichimura, S. Kuwahara, F. H'Dhili, K. Uetsuki, Y. Okuno *et al.*, *Nature communications* **4**, 2592 (2013).

[9]. Y. Okuno, Y. Saito, S. Kawata, P. Verma, *Physical review letters* **111**, 216101 (2013).

[10]. M. S. Sselhaus, A. Jorio, R. Saito, *Annual Review of Condensed Matter Physics* **1**, 89-108 (2010).

[11]. M. S. Dresselhaus, G. Dresselhaus, R. Saito, A. Jorio, *Physics reports* **409**, 47-99 (2005).

[12]. A. Jorio, R. Saito, J. Hafner, C. Lieber, M. Hunter, T. McClure *et al.*, *Physical Review Letters* **86**, 1118 (2001).

[13]. H. Farhat, H. Son, G. G. Samsonidze, S. Reich, M. Dresselhaus, J. Kong, *Physical review letters* **99**, 145506 (2007).

[14]. K. Sasaki, R. Saito, G. Dresselhaus, M. S. Dresselhaus, H. Farhat, J. Kong, *Physical Review B* **77**, 245441 (2008).

[15]. K.-i. Sasaki, H. Farhat, R. Saito, M. S. Dresselhaus, *Physica E: Low-dimensional Systems andNanostructures* **42**, 2005-2015 (2010).

[16]. F. Tuinstra, J. L. Koenig, *The Journal of Chemical Physics* **53**, 1126-1130 (1970).

[17]. K. Sato, R. Saito, Y. Oyama, J. Jiang, L. Cançado, M. Pimenta *et al.*, *Chemical physics letters* **427**, 117-121 (2006).

[18]. M. Dresselhaus, A. Jorio, R. Saito, *Annu. Rev. Condens. Matter Phys.* **1**, 89-108 (2010).

[19]. F. J. Boerio, S. K. Bahl, G. E. Mcgraw, *J. Polym. Sci.; (United States)* **14**, 1029-1046 (1976).

[20]. J. M. Pitarke, V. M. Silkin, E. V. Chulkov, P. M. Echenique, *Reports on Progress in Physics* **70**, 1-87(87) (2007).

[21]. A. V. Zayats, I. I. Smolyaninov, A. A. Maradudin, *Physics Reports* **408**, 131–314 (2005).

[22]. E. C. L. Ru, E. Blackie, M. Meyer, P. G. Etchegoin, *J.phys.chem.c* **111**, 13794-13803 (2007).

[23]. S. Keren, C. Zavaleta, Z. Cheng, A. de La Zerda, O. Gheysens, S. Gambhir, *Proceedings of the National Academy of Sciences* **105**, 5844-5849 (2008).

[24]. Y. Peter, M. Cardona, *Fundamentals of semiconductors: physics and materials properties*. (Springer Science & Business Media, 2010).

Chapter 3.

Raman study on Ag coated laser-structured RGO stripes

In this charpter, multilevel Ag coated laser laser-fabricated RGO structures is introduced. In details, two-beam laser interference (TBLI) was utilized. Through a laser induced ablation and photoreduction process, hierarchical graphene structures with microscale gratings and nanoscale folders were achieved. The hierarchical structures contribute to the formation of plasmonic structures after silver coating by simple physical vapor deposition (PVD). When applied for Raman study, the dispersed AgNPs gave rise to the formation of plenty of SERS "hot spots". In the detection of Rhodamine B (RhB), this multilevel structures showed high SERS enhancement and good reproducibility, a detection limit of 10^{-10} M has been achieved.

3.1 RGO micro-nanostructures fabrication for chemical sensor

In recent years, 2D graphene materials has attract more and more researchers' interest, for it not only posses many extraordinary properties but also has the potential for new device applications [1, 2]. Its derivations such as GO and RGO also became more and more famous, even their properties are not as perfect as pure graphene. However, GO or RGO materials are much easier to produce and more suitable for real application. Recently, they showed addition potential in SERS investigation due to the fluorescence

quenching effect, an additional SERS chemical enhancing ability, high adsorption to target molecules, very good biocompatibility and anti-oxidation of silver nanoparticles [2-4]. Thus, rational combination of GO/RGO and noble metal NPs could dramatically improve the conventional SERS performance in various aspects. Traditional methods usually just simply combined GO or RGO layers with metallic particles [3, 4], the enhancement was relative low, the reproducibility was also not satisfied. Here, to improve that situation, silver coated laser-structured RGO stripes is introduced.

The GO films were prepared by using or improved Hummers' method [5]. The basic principle of Hummers' method is illustrated in Figure 3.1. As first step, natural graphite is oxidized into graphite by the treatment with various oxidants in acidic media (such as $KMnO_4$, H_2SO_4, or benzoyl peroxide [7]). Then graphite oxide is exfoliated into graphene oxide sheets in water by ultra-sonication, and forms a uniform turbid liquid. The GO material can be purified by high-speed centrifugation and dialysis to remove inorganic impurities such as metal ions and acids. The purified GO could finally be reduced through chemical reduction [8-11] or laser induced reduction [12-14].

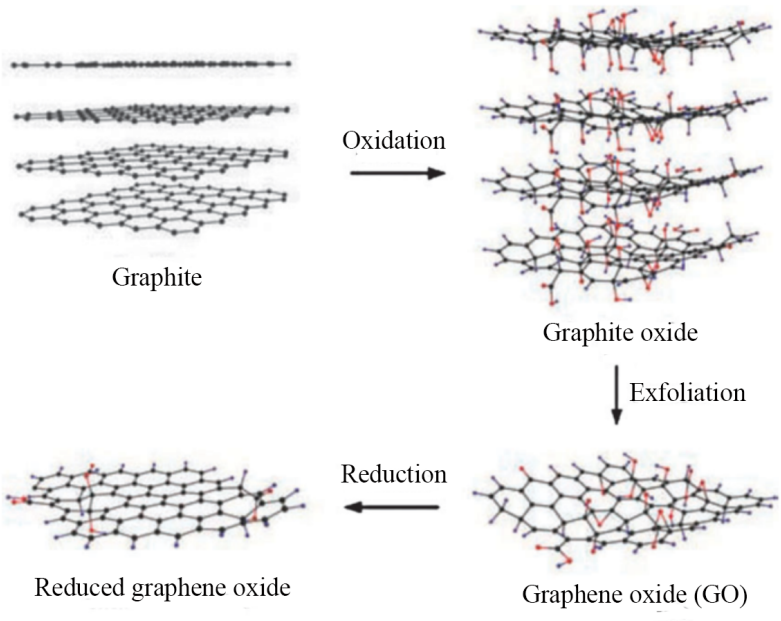

Figure 3.1 Scheme of Hummers' method for RGO preparation from graphite [6].

In this research, the high quality GO material was prepared from purified natural graphite (Aldrich, <150 um), then the GO film was obtained from spin coating the GO turbid liquid on a piece of cover glass. The detail procedurals are illustrated as follows.

Purifying GO material:

1. At 0°C (in thermostatic pot in ice water mixture), take 2g natural graphite, 2g sodium nitrate ($NaNO_3$), 96ml concentrated sulfuric acid (H_2SO_4) and mix them in a beaker.

2. Keep the system temperature at 0°C, slowly add 12g mineral chameleon ($KMnO_4$).

3. Keep stirring the mixture at 0°C for 90min, then heat the system to 35°C and mix it for 2h.

4. Dilute the mixture by slowly injecting 80ml-deionized water in 30min.

5. Inject 10ml peroxide (30%) to the turbid liquid, followed by inputting 200ml deionized water, keep stirring for 10min and get turbid liquid of graphite oxide.

6. Centrifuge the mixture with high speed (16000 rpm) for 10min, and separate graphite oxide from the turbid liquid. Continue centrifuging and cleaning the rest of the turbid liquid with deionized water until the PH reaches 7.

7. Using ultrasonic wave treat the mixture, further separate the graphite oxide and get turbid liquid of GO.

8. Centrifuge the mixture with high speed (16000 rpm) again for 20min, separate GO and dry it in the vacuum chamber at 90°C to get pure dry GO for further using.

Preparation of GO film:

1. The as-prepared GO material (in the form of small flakes) is first made into GO turbid liquid with a concentration of 3mg/ml by inputting deionized water and dispersing by ultrasonic wave. As the GO was purified, its dispersion in the liquid is

uniform. The turbid liquid shows semitransparency with a color of brown yellow, and proves to be stable even putting still for long time.

2. Clean cover glasses as templates for GO film. Consequently, clean the glass with acetone, ethanol and ultrasonic wave, finally wash them with deionized water and dry them.

3. Drop one droplet of GO turbid liquid onto one piece of cover glass, then spin coat it with 1000rpm for 30s, dry it in in air at room temperature. One can get the aimed film thickness by trying different spin-coating times.

4. The GO films are OK for further structures fabrication and reduction. If special function needed, such as for microelectronic devices fabrication, pre-metal coating or other treatment is essential.

Two-beam laser interference (TBLI) patterning

The GO films are used for fabrication of graphene stripes by TBLI system. The scheme of the TBLI system is illustrated in Figure 3.2.

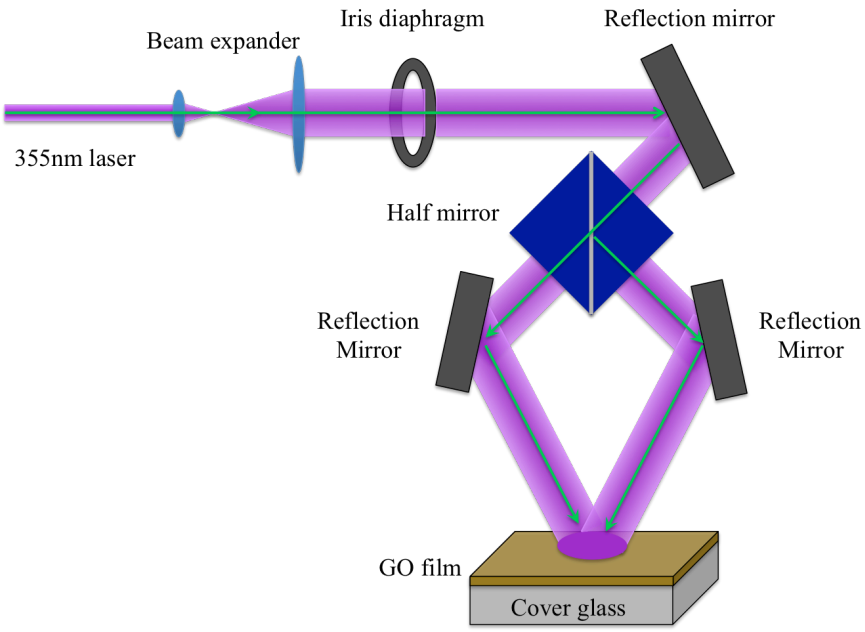

Figure 3.2 Scheme of TBLI system used for RGO structures fabrication.

In the TBLI system, a frequency-tripled, Q-switched, single-mode Nd:YAG laser (Spectra-Physics) was utilized. The emission wavelength was 355nm, the laser pulse frequency was 10 Hz and the pulse duration was 10 ns. The beam diameter was 9 mm, which was adjusted by the beam expander. And then it was split into two beams, which had the same optical path length to the sample and interfered on the surface of the GO film.

To give an intuitionistic image of the interference pattern, the laser intensity distributions on the interference area were theoretical simulated by Matlab, as shown in Figure 3.3. The periodic distribution of laser intensity along x direction is obviously observed, while keeps same along y direction. Due to the calculation, the strongest intensity of the interfered pattern is 4 times of that of single laser beam and the lowest intensity is 0. So when interacts with laser active material substrates, large area periodic patterns according to the intensity distribution will be available, such as stripes. Here there are two important factors that will affect the pattern qualities, one is the laser intensity which should neither be too strong nor too weak; the other is the period of the stripes which could be well adjusted by tuning the intersection angle.

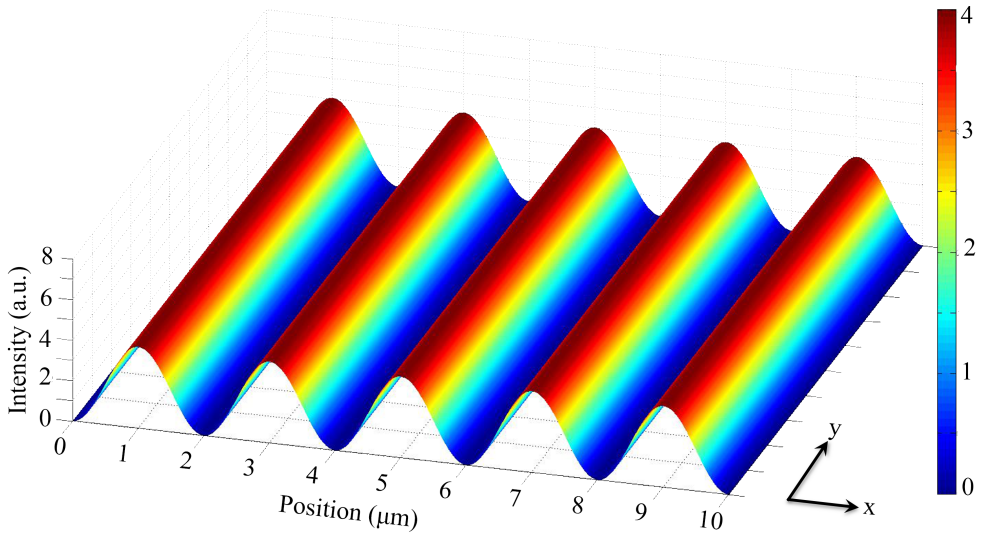

Figure 3.3 Laser intensity distribution of the two-beam interference

Multilevel plasmonic structure fabrication

Graphene stripes could be fabricated by exposing the GO film to the laser interference region for several second. During this process, there were two kinds of reactions happened between the laser and GO film. They are laser ablation and laser induced reduction.

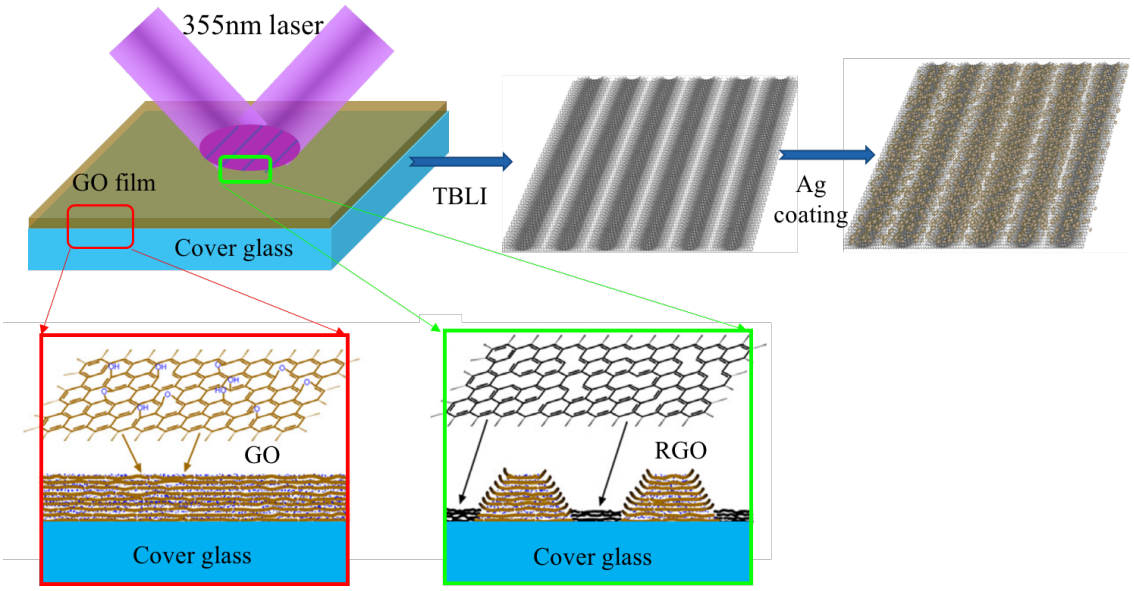

Figure 3.4 Scheme of Ag-RGO structures fabrication by TBLI treatment and Ag coating. The figures in red and green square illustrate the cross-section of GO film and TBLI treated RGO/GO structures respectively.

When illuminated under the strong stripes region of the interfered laser (as shown in Figure 3.3), GO material would absorb the laser energy, generate heat and break chemical bonds. That is because the 355 pulse laser intensity was strong enough to over the chemicals bond energy. As this process was carried out in the atmospheric environment, the GO film would be thinned and generate CO_2 and CO, as shown in Figure 3.4. This is the laser ablation process.

While at the neighbor part of the strong interfered stripes, where the laser intensity is not so strong to ablate GO, but still higher enough to break the weak bond between the

oxygen functionalities and graphene layers. The oxygen functionalities would be removed in the form of CO_2 or CO gas, and left so called reduced graphene oxide layers. This is the laser reduction process. Here we should notice that at the thinner part of the RGO structures in Figure 3.4, it is laser treated GO film. This part is made of less RGO layers, where the laser consumed much energy on ablating the upper part GO and left less energy to reduce the lower thin part GO.

The scheme of side view of RGO structures is shown in Figure 3.4, the interesting phenomena is that at the edge part of the GO stripes (not ablated part), the RGO layer edges are dispersed. That was generated by the CO_2/CO gas expansion force during the GO reduction process [15, 16]. And the dispersed RGO layers would play an important role for guiding the AgNPs growth.

To fabricate a sensitive SERS substrates based on the graphene stripes, silver was coated using thermal evaporation system DM-300B. The procedure is shown in Figure 3.4. The Figures in red and green square show the cross-section of GO film and TBLI fabricated RGO/GO structures. During TBLI treatment, the strong laser stripes interact with GO film, both laser ablation and reduction will happen. Due to the ablation process, part of GO film would be incinerated; while part of GO would be reduced and generate RGO layers. At the edge part of GO stripes, the edges of RGO layers form nanoscale fine structures, which contribute to guiding AgNPs growth with uniform size and arrangement. This will help forming large amount of hotspots when used as SERS substrates. In Figure 3.4, the Ag deposition was carried out by physical vapor deposition (PVD) using thermal evaporation system DM-300B, in a high vacuum (less than 5×10^{-4} Pa), with a low deposition rate at 0.03nm/s, and the final thickness was about18nm.

3.2 SERS characterization of Ag-RGO substrate

The morphology of the multilevel structure

During TBLI fabrication, the GO film was exposed to the interfered laser beams, after which GO surface was treated in a similar pattern as the intensity distributions. The region exposed to high laser intensity could be partially ablated and reduced to RGO [12-16], whereas, the region under low intensity survived. The morphology of the RGO/GO surface was characterized by scanning electron microscopy (SEM) by using a field-emission scanning electron microscope (JSM-7500F, JEOL, Japan). The optical and SEM images of RGO stripes are shown in Figure 3.5.

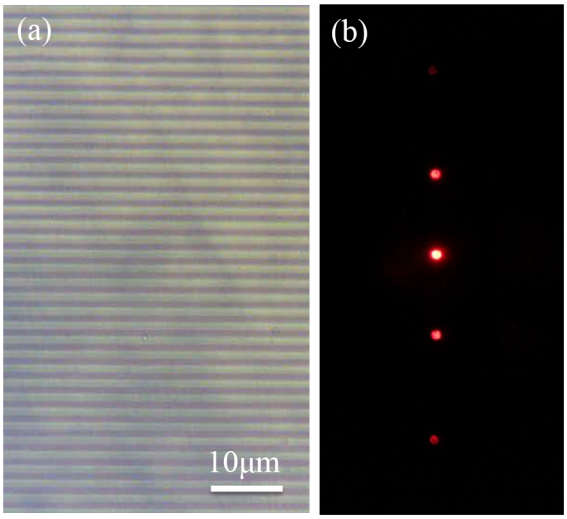

Figure 3.5 (a) Optical image of RGO stripes fabricated by TBLI. (b) Diffraction pattern of the RGO stripes.

As shown in Figure 3.5 (a), after TBLI treatment, stripes structures have been created. The period of stripes is about 2 μm, which could be clearly observed by optical microscope. Particularly, the period of ~2 μm was found to be suitable for achieving super-hydrophobicity, which has been confirmed in our previous works, so other periods have not been adopted for the fabrication of SERS substrates in this work. What is more, the periodic structure could be confirmed by diffraction tests. Figure 3.5

(b) shows the diffraction pattern, which suggests that the periodic stripes are very uniform. Notably, the uniform structure is a very important character for the SERS substrates, since it would guarantee a high reproducibility in real SERS detection.

To investigate the details of the surface structures of RGO stripes, scanning electron microscope (SEM) was carried out as shown in Figure 3.6. Figure 3.6 (a) and (b) show the SEM image of the RGO stripes and the magnified SEM image of the area marked by red square in Figure 3.6 (a), which shows the details of the RGO stripes structure. We noticed that, in addition to micro-scale stripes, there exist special nanofolder structures at the edge part of each stripe.

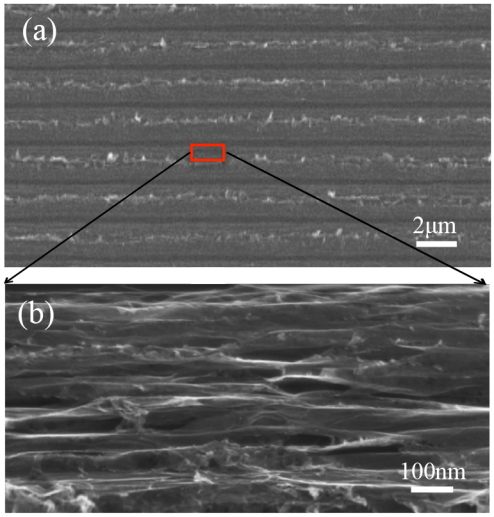

Figure 3.6 (a) SEM image of the RGO stripes fabricated by TBLI. (b) Magnified SEM image of the red square marked in (a).

The formation of nanoscale layered structure could be attributed to the laser treatment induced reduction and the emission of carbon species (e.g., CO and CO2). As we know that both the microscale stripe and the nanoscale nanofolder of the resultant RGO surfaces would lead to a rough surface, which is benefit the plasmonic structures formation. This rough surface combined with the resultant RGO nanofolders shows unique superhydrophobicity, which will be particularly discussed in next section.

Using the fabricated RGO stripes as templates, sensitive SERS substrates could be fabricated by simply coating a thin layer of silver nanoparticles using a PVD technique. Figure 3.7 shows the SEM images of silver coated RGO (Ag-RGO) stripes, the hierarchical structures have not changed after decoration with silver. The microscale stripes as well as nanoscale layers could be clearly identified from the SEM image.

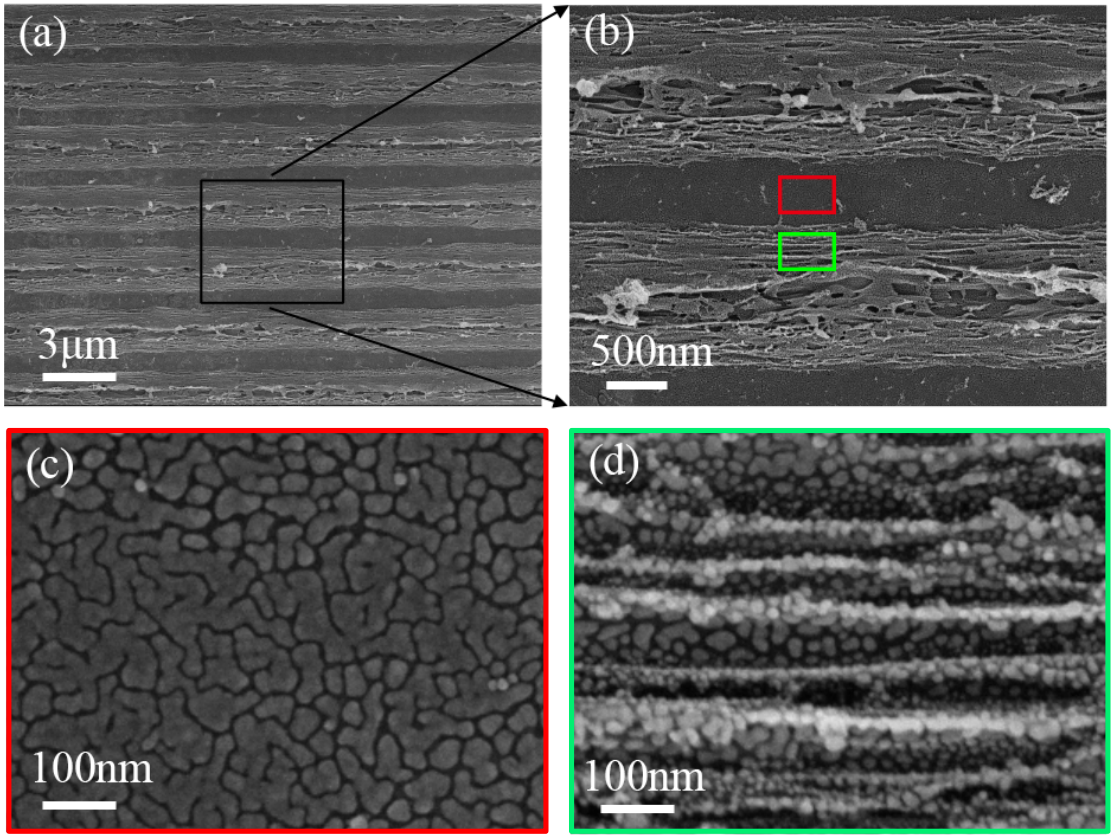

Figure 3.7 (a) SEM images of Ag-RGO stripes. (b) Magnified SEM image at the square area marked in (a). (c) & (d) Magnified SEM images of the area marked by red and green squares in (b) respectively.

To get further insight into the morphology of silver layer, the SEM image was further magnified. As shown in Figure 3.7 (c) and (d), we observed both the flat region (RGO strips) and the structured region marked by red and green squares, respectively. On the flat region, Ag nanoislands were uniformly deposited on the RGO surface and connected together; whereas on the structured region, the nanoscale layers could separate the Ag nanoparticles by providing large substrate contact region. Silver nanoparticles with smaller particle size (10-30 nm) well disperse over the entire

nanofolder structures homogeneously (Figure 3.7 d). The nanoscale gaps (1~2 nm) between silver nanoparticles together with the AgNPs could be considered as plasmonic structures, which contribute to the enhancement of electromagnetic field. As compared with the Ag nanoislands in the flat RGO region, stripes-structured RGO substrate would generate plenty of SERS "hot spot" after silver coating and contribute to the SERS detection performance accordingly.

To get sufficient localized "hot spot", plenty AgNPs is crucial, which needs enough silver thickness during PVD process; while too much quantity silver should also be avoided to refrain from forming big Ag grains or continued Ag layer. Due to our experience, a layer thickness around 20nm is proper. The thickness of the silver layer was measured by atomic force microscopy (AFM, iCON, Veeko) as shown in Figure 3.8. A thickness of 18nm silver layer on a flat substrate was confirmed.

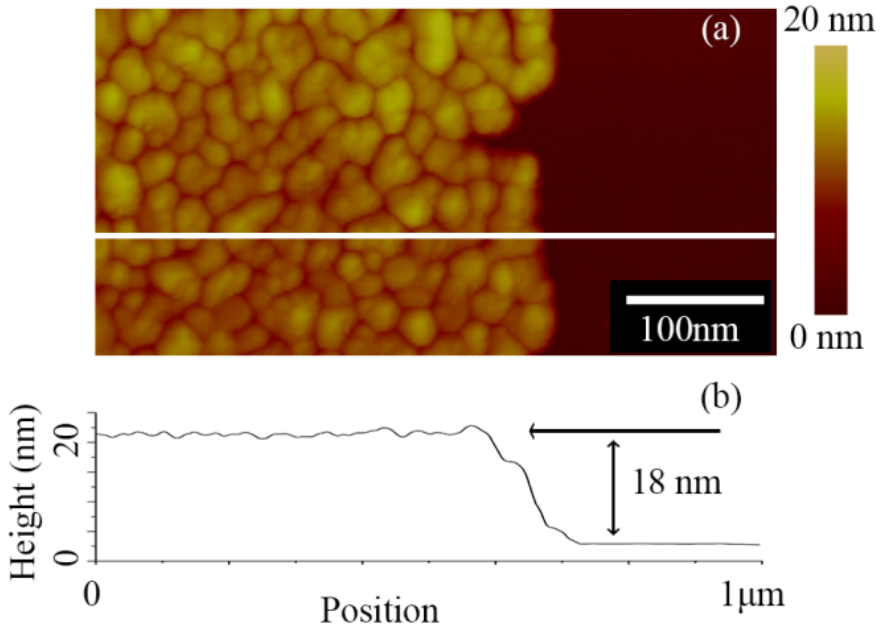

Figure 3.8 (a). AFM image of the Ag coated GO substrate. (b). AgNPs thickness measurement along the white line in (a).

Super hydrophobicity of Ag-RGO stripe structures

In addition to the electromagnetic field enhancement that originated from the plasmonic structures, the presence of graphene could also give rise to Raman enhancement by means of chemical interaction with the detected molecules, which is called chemical enhancement [17, 18]. The unique dewetting property would contribute to the enrichment effects, so-called condensation effect, which can also further lower the SERS detection limit. Recently, rough metal surface has also been prepared by coating silver or gold nanoparticles on rough templates, such as DVD disk, paper and even rose petal [19-21].

Here, the superhydrophobicity was characterized by the contact angle of the Ag-RGO stripes, which was checked by dropping a drop of RhB solution on the Ag-RGO stripes SERS substrate. As shown in Figure 3.9 (a), the CA was measured to be ~152º. The CA of RGO stripes and pure AgNPs were also checked, as shown in Figure 3.9 (b) and (c) respectively. The slightly increased CA compared with that of RGO stripes (~150º) and pure Ag NPs coated cover glass substrate (~107º) could be attributed to the increased surface roughness after silver coating on the nanoscale RGO stripes [22].

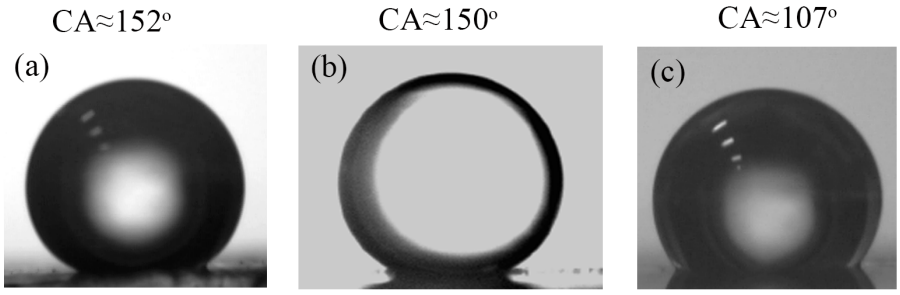

Figure 3.9 CA of (a) Ag-RGO stripes, (b) RGO stripe without Ag and (c) Ag nanoparticles coated GO film without stripe structures.

Importantly, the sphere shaped RhB droplet has a significantly decreased contact area with the substrate (Ag-RGO stripes). In our experiment, the RhB drop was evaporated naturally in ambient condition. We recorded the photographs of the droplets during the

evaporation process, as shown in Figure 3.10 (b-d), the droplet became smaller and smaller, the contact area almost keeps a consistent value. In other words, all of the RhB molecules in the 4 μL droplet were deposited within the contact area, about 0.9 mm^2. For comparison, we also measured a hydrophilic glass surface that has a low CA of ~15º, the contact area between the glass surface and a 4-μL droplet is measured to be 12.5 mm^2. Form this point of view, the superhydrophobic Ag-RGO stripes substrate would lower the SERS detection limit to more than one order of magnitude.

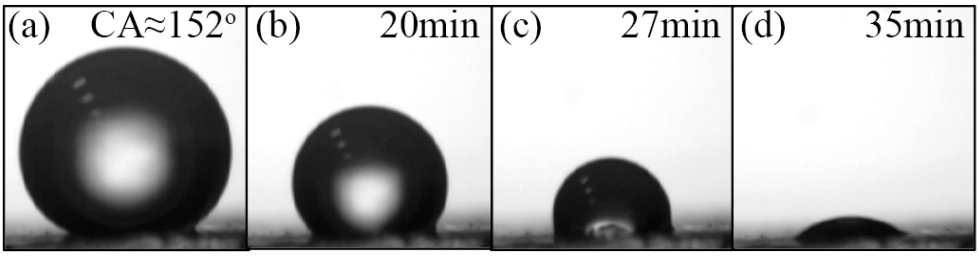

Figure 3.10 (a-d) The optical images during the evaporation of the RhB droplet. In (a) the original CA was measured to be ~152°. The images were recorded after evaporation for different times.

In order to check the Raman performance of the Ag-RGO stripes structures, RhB was chosen as Raman probe material and the as fabricated SERS substrate-based Raman measurement was conducted.

Raman spectra were recorded on a LabRAM HR Evolution from Horiba scientific equipped with a He-Ne laser at 633 nm as excitation source, the laser power was about 30uW on the samples, and the average spot size was 1 μm in diameter. The objective is 100x with a NA of 0.8. The optical setup is illustrated in Figure 3.11.

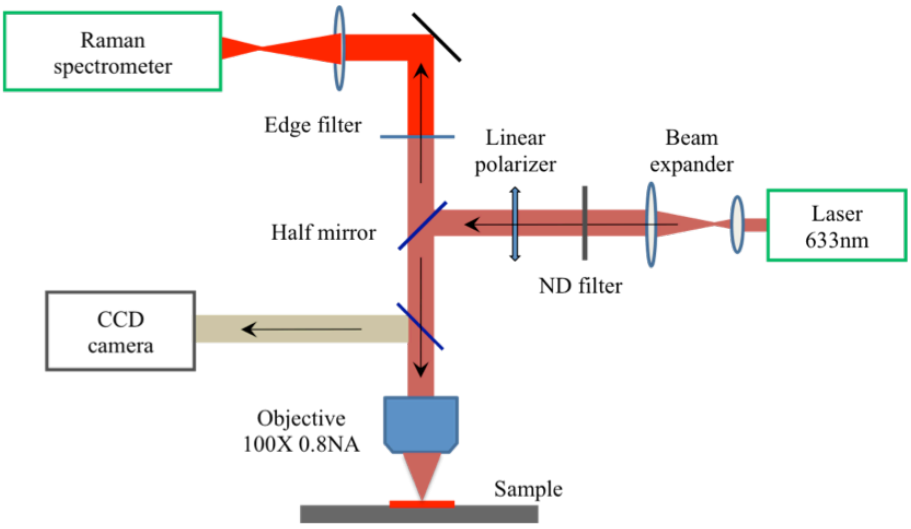

Figure 3.11 Scheme of Raman system (LabRAM HR Evolution).

Enhanced Raman on Ag-RGO structures

As the SERS substrate contains two different types of surface morphology, as shown in Figure 3.12 (b). On the flat region, it was Ag coated complanate RGO layer. The AgNPs there were big, not uniform and with iregular shape. These properties are not good for getting high enhancement and good reproducibility. While on the structured region, it was Ag coated RGO/GO nanofolders. The AgNPs are relative uniform with a size of 15nm. They closed packed along the RGO layer edges, the gaps between them was around 1nm. When illuminated with light, the AgNPs can generate plenty of hot spots. The SERS performance were confirmed on these two different places. As shown in Figure 3.12 (a), the Raman enhancement on the structrued region was about 5 times higher than that on the flat region. This result agreed well with the different plasmonic structures. The later SERS measurements were all conducted on the structured region.

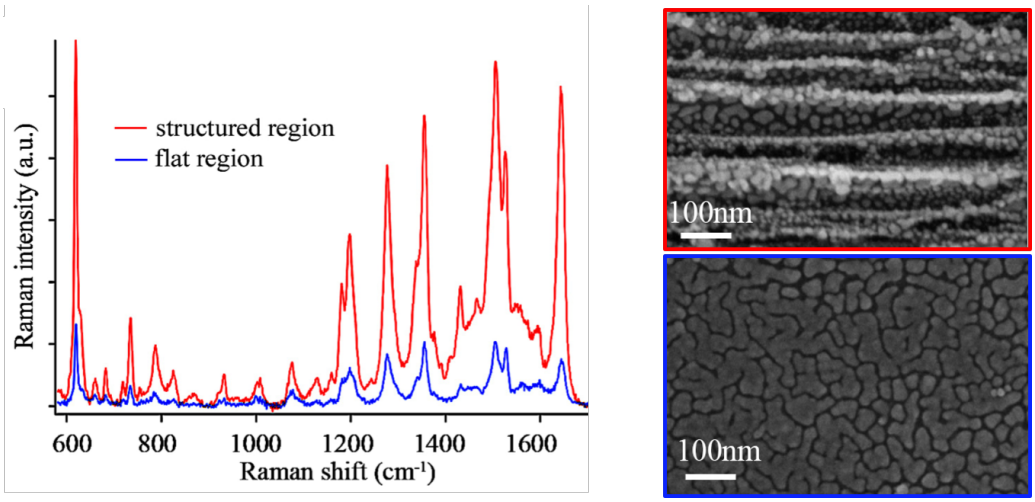

Figure 3.12 (a) SERS of RhB solution (10^{-6} M) measured on flat (blue curve) and structured (red curve) region on Ag-RGO substrate. (b) SEM of flat (in blue square) and structured region (in red square).

Polarization dependence confirmation

To evaluate the SERS performance of Ag-RGO stripes substrate, we used RhB as a probe molecule for Raman detection. Since the unique stripe structure shows obvious anisotropic properties, we first checked the SERS performance with different laser polarization directions. In this test, the concentration of RhB was 10^{-6} M, the directions of the laser polarization are illustrated in Figure 3.13 (inset) with respect to the stripes direction, and we compared the SERS signal of linear polarized laser that parallel and perpendicular to the stripes, as shown in Figure 3.13 (a).

It was obvious that when the laser polarization direction was parallel to the stripes, the Raman signal was almost twice stronger than that along the perpendicular direction. By carefully observing the AgNPs decorated on the RGO layers, it could be explained as that when the laser polarization is parallel to the stripes, most of the AgNPs packed in same layer could interact with each other and generate strong localized SPPs; while on the other hand, when the laser polarization is perpendicular to the stripes, the SPPs were mainly generated from AgNPs that separated by the RGO layers, and thus provided relative weaker E-field enhancement. Thus this structures would help

increasing the laser coupling efficiency. The simulation results were also conducted, which strongly support the experiment result, as shown Figure 3.13 (b). In this regard, the SERS measurements in the following experiments were all implemented with the laser polarization parallel to the stripes' direction.

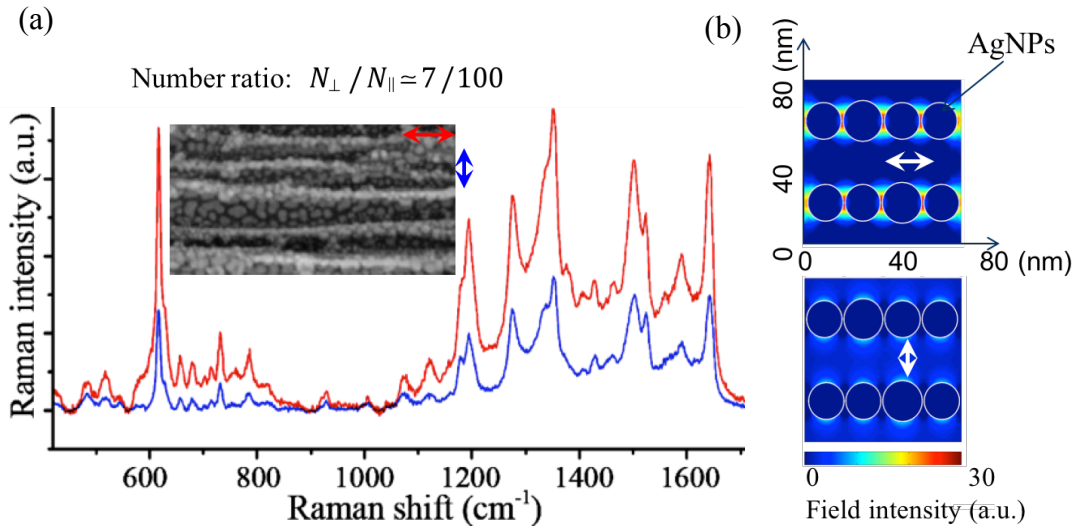

Figure 3.13 (a) Comparison of SERS measured with two different laser polarization directions with respect to the stripes, red and blue curves show the SERS spectra measured with the polarization parallel and perpendicular to the stripes, respectively; inset is the SEM image of the Ag-RGO stripes. (b) Simulation result of the intensity distribution of AgNPs with laser polarization parallel (upper) and perpendicular (lower) to the RGO stripes

To further confirm the multilevel structures contributions for SERS, we decreased the RhB concentration to 10^{-10} M, and compared the Raman spectra on Ag-RGO stripes, bare RGO stripes and Ag coated flat GO film, respectively. As shown in Figure 3.14, compared with Ag-RGO stripes substrate, both RGO stripes without Ag and Ag coated flat GO film show very weak Raman enhancement under the same excitation conditions. This result showed the unique advantages of the combined structures of both RGO nano-folders and the well-dispersed AgNPs. Also even for the the low concentration sample (10^{-10} M), the characteristic Raman peaks (at 611, 1360, 1507 and 1651 cm^{-1}) could be clearly observed. The excellent SERS performance could be

attributed to the combined structures of both RGO stripes and the well-dispersed AgNPs.

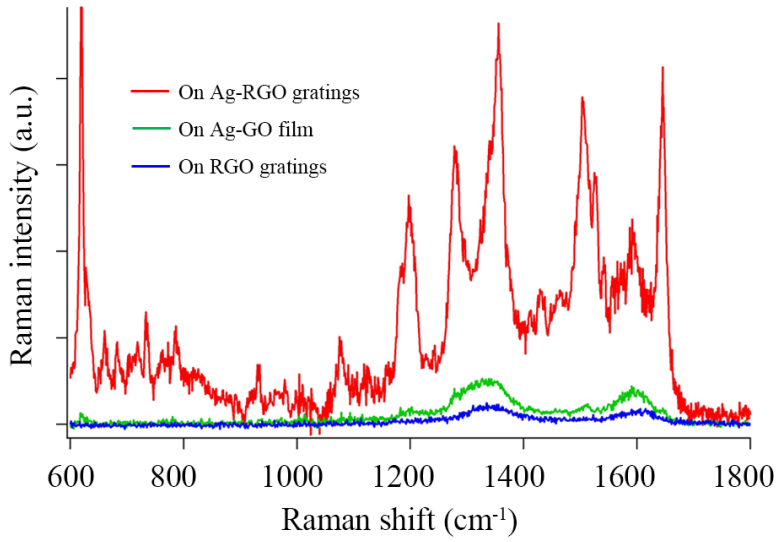

Figure 3.14. Comparison of Raman spectra of 10^{-10} M RhB measured on the substrate with Ag-RGO stripes (red curve), Ag coated GO film (green curve) and pure RGO stripes (blue curve)

Enhancement factor calculation

To give another direct proof of SERS substrate performance, we calculated the enhancement factor (EF) of our SERS substrates. Here we noticed that for the same low concentration of RhB, the normal (non-enhanced) Raman signal was too weak to compare with the SERS signal, thus we use higher concentration (10^{-4}M) RhB for normal Raman signal testing and lower concentration (10^{-10}M) for SERS signal taking (In this paper, in order to protect the SERS substrate and the RhB molecules, we didn't use high exciting power and long exposure time, for both cases the laser power was 30μw and exposure time was 20s). The comparison of SERS signal and Raman signal of RhB is shown in Figure 3.15.

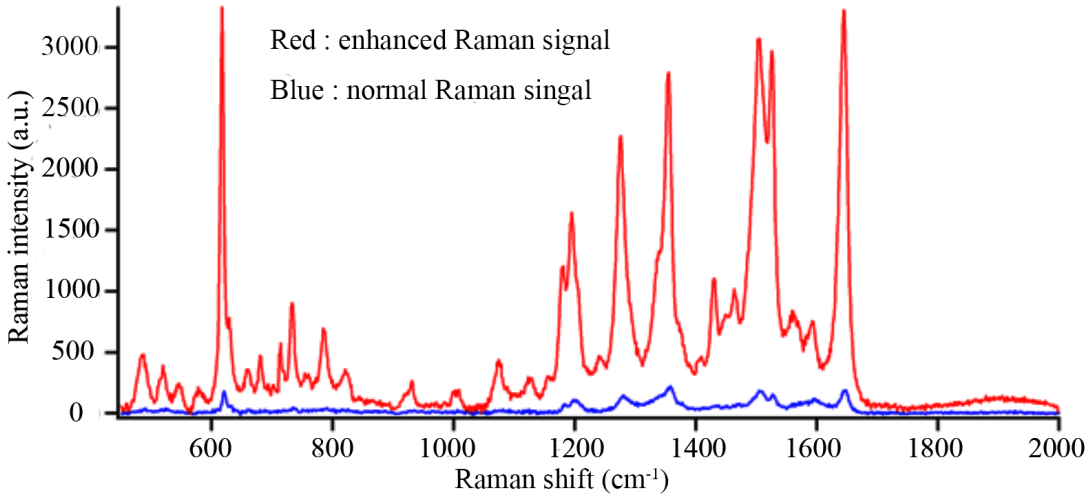

Figure 3.15 Comparison of SERS signal of 10^{-10}M RhB on Ag-RGO stripes substrate (red curve) and normal (non-enhanced) Raman signal of 10^{-4}M RhB on bare RGO stripes substrate (blue curve).

We used the equation $EF = \frac{I_{SERS}/N_{SERS}}{I_{vol}/N_{vol}}$ to calculate the enhancement factor, where I_{SERS} is the SERS peak intensity, I_{vol} is the normal Raman peak intensity, N_{SERS} is the average number of adsorbed molecules in the scattering volume for the SERS measurements, N_{vol} is the average number of molecules in the Raman scattering volume. Here $N_{SERS} = C_{SERS} V \frac{S_{SERS}}{S_0}$ and $N_{vol} = C_{vol} V \frac{S_{vol}}{S_0'}$, where C_{SERS} and C_{vol} are the sample concentration used for SERS and normal Raman respectively, V is RhB solution volume. As the sample is on solid surface, $S_{vol} = S_{SERS}$, is the laser focus area for Raman excitation, S_0 and S_0' are the contact area between the RhB solution and Ag-RGO and RGO stripes substrate respectively, as the contact angle of Ag-RGO and RGO stripes are similar, we assumed that $S_0 \approx S_0'$. Finally EF can be written as: $EF = \frac{I_{SERS}/C_{SERS}}{I_{vol}/C_{vol}}$, while $C_{SERS} = 10^{-10}$M and $C_{vol} = 10^{-4}$M. Thus $EF = \frac{I_{SERS}}{I_{vol}} \times 10^6$, we

chose the peak intensity at 611, 1360, 1507 and 1651 cm^{-1} (see Figure 3.14), then calculated ratio of I_{SERS}/I_{vol} and got EF value, which is about 2.0×10^{7}. In contrast with other researchers' works, this value is comparable [25-27], and the high enhancement factor strongly supports that nice SERS performance of the Ag-RGO stripe structures.

3.3 SERS Reproducibility of Ag-RGO structures

For SERS substrates, the signal reproducibility is a very important factor that affects their performance and reliability. In this section, we evaluated the reproducibility of the SERS signals of our Ag-RGO stripes SERS substrate in the detection of RhB solution with concentrations of 10^{-10} M and 10^{-6} M, respectively. For each sample, we chose 7 different positions randomly on the Ag-RGO stripes. As shown in Figure 3.16 (a) and (b), even at a concentration of 10^{-10} M, the Raman spectra also showed very high uniformity and low fluctuation, the case was the same in the detection of RhB solution at a concentration of 10^{-6} M, indicating the high reproducibility of our Ag-RGO stripes substrate. As a direct proof of the remarkable reproducibility, Figure 3.16 (c) and (d) show the Raman signal fluctuation at band 1360 cm^{-1} of RhB with 10^{-10} M and 10^{-6} M, respectively. It is much clearer to judge the signal stability, and we calculated the relative standard deviation (RSD) as 10.4% for the 10^{-10} M and 8.0% for the 10^{-6} M sample, respectively. The low RSD values indicate the excellent SERS signal reproducibility of the Ag-RGO stripes substrate.

Here, the little differences between the RSD values of two samples were due to the low signal to noise (S/N) ratio of the low concentration (10^{-10} M) sample, where the noise signal float could somehow affect the signal fluctuation. The highly reproducible SERS signals could be attributed to the uniformity of the stripe structures. It is necessary to point out that we measured all the SERS signals on the structured region of the stripes.

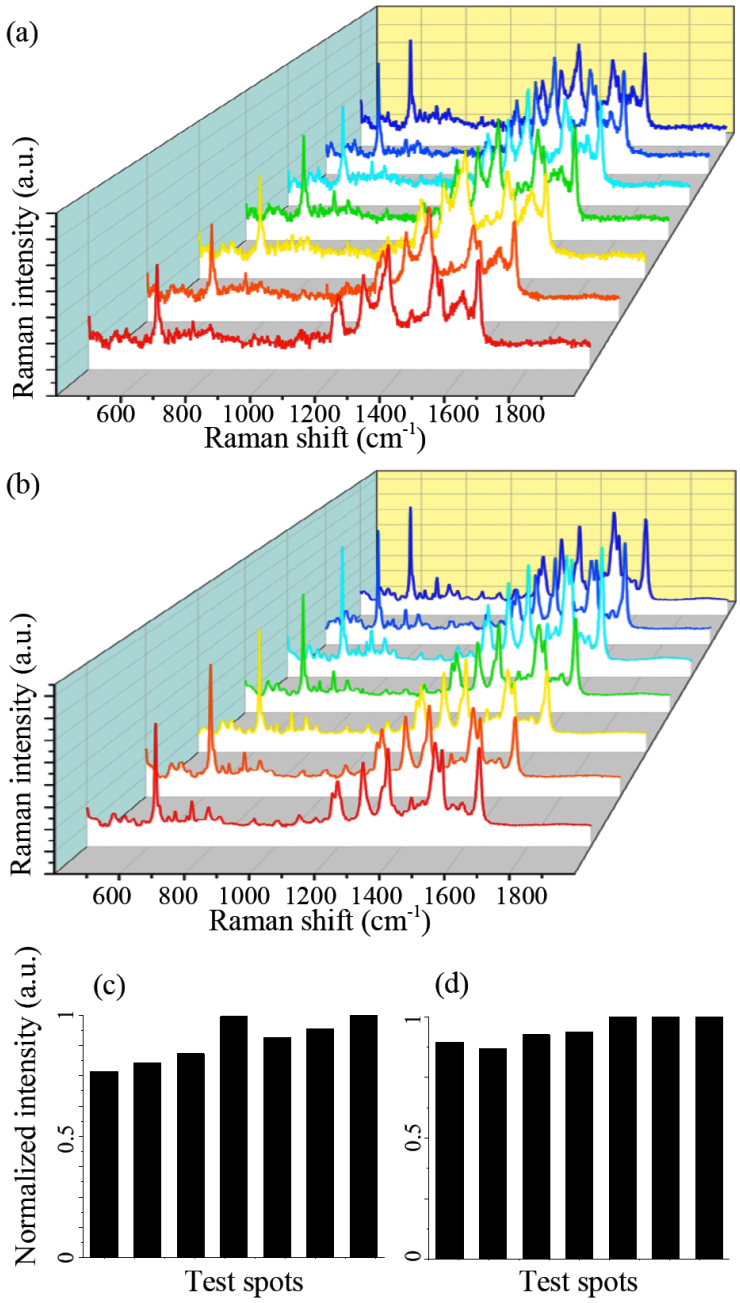

Figure 3.16 Raman spectra of RhB with a concentration of (a) 10^{-10} M and (b) 10^{-6} M at 7 different positions, respectively. The peak intensity of the Raman mode at 1360 cm^{-1} on 7 measured sites of (c) 10^{-10} M and (d) 10^{-6} M samples, respectively

As a complemental support, SERS signals of RhB (10^{-6} M) on 4 different pieces of substrates were also collected and compared, in which high reproducibility (RSD=8.3%) has been achieved (Figure 3.17).

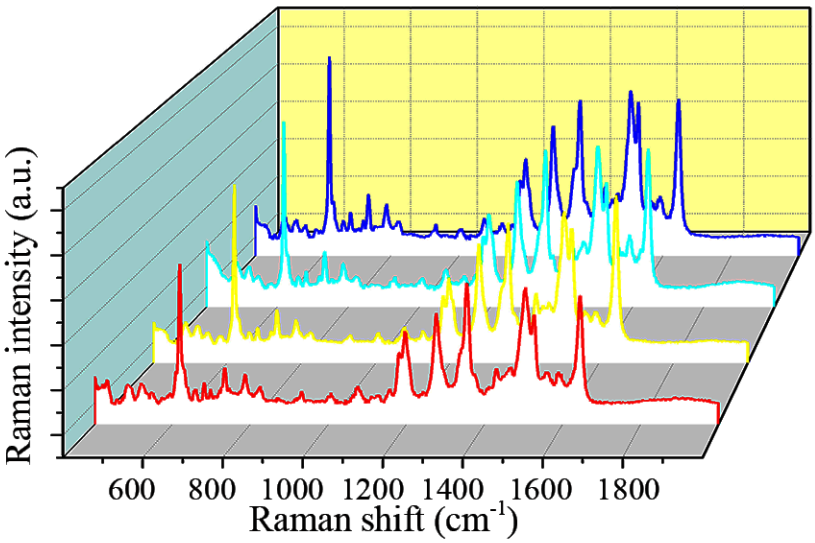

Figure 3.17 Raman spectra of RhB (10^{-6} M) at 4 different pieces of substrates.

Additionally, it is well known that one of the major problem of using silver plasmonic structures is the silver oxidation, which is important since it will affect the temporal stability and therefore also reproducibility in time of the system. Thus to evaluate the stability of SERS substrate, we checked the SERS performance vs time at one fixed substrate position, as shown in Figure 3.18. Due to the result, even after 3 weeks, the SERS performance did not change much, just slightly decreased (~4.7%). In fact, this is not abnormal, we also checked with other papers [23, 28, 29], in which the silver oxidation did not affect the SERS performance much.

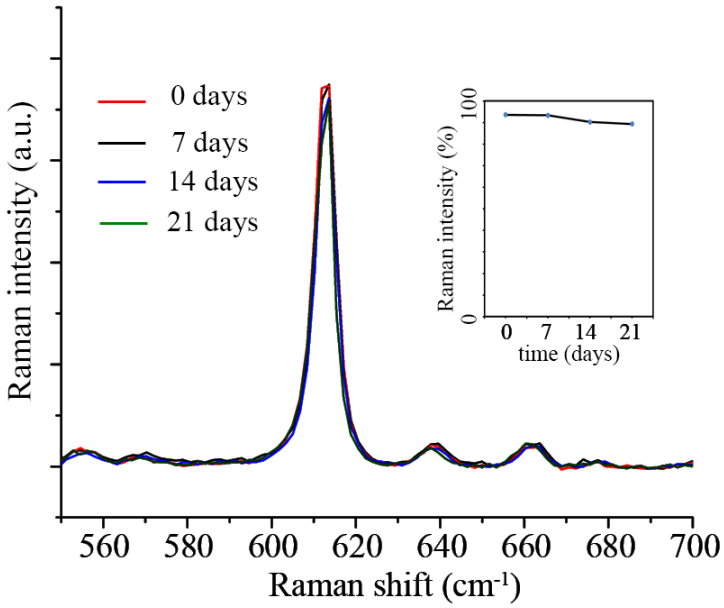

Figure 3.18. Raman signal at same spot measured at different time (0, 7, 14, 21 days later respectively marked by different colors). Inset is the Raman intensity (at 612cm^{-1}) changes vs time.

Summary

In this chapter, I have introduced the development of a multilevel structures by combining TBLI fabrication of RGO stripes with PVD coating of silver. In details, Hummers' method was used for the GO material preparation. And TBLI method was illustrated. Finally, Raman spectroscopy was carried on the RGO stripes-based hierarchical micronanostructures. This multilevel surface showed high Raman enhancement with an enhancement factor around 2x10^{7}. The hierarchical structures not only contribute to the enhancement of local electromagnetic, but also lead to superhydrophobicity induced enrichment effect, which further lowers the detection limit of target analytes. By using the Ag-RGO stripes as substrate for Raman spectroscopy, the enhanced Raman detection limit as low as 10^{-10} M has been achieved, and the SERS signals on different positions together with the less-time dependence of the substrate showed both high special and temporal reproducibility. TBLI fabrication of RGO stripes may hold great promise for the development of highly efficient SERS substrates.

References:

[1]. M. J. Allen, V. C. Tung, R. B. Kaner, *Chemical reviews* **110**, 132-145 (2009).

[2]. Y. Zhu, S. Murali, W. Cai, X. Li, J. W. Suk, J. R. Potts *et al.*, *Advanced materials* **22**, 3906-3924 (2010).

[3]. W. Fan, Y. H. Lee, S. Pedireddy, Q. Zhang, T. Liu, X. Y. Ling, *Nanoscale* **6**, 4843-4851 (2014).

[4]. W. Ren, Y. Fang, E. Wang, *ACS nano* **5**, 6425-6433 (2011).

[5]. W. S. H. Jr, R. E. Offeman, *Journal of the American Chemical Society* **80**, (1958).

[6]. B. Hua, L. Chun, S. Gaoquan, *Advanced Materials* **23**, 1089–1115 (2011).

[7]. J. Shen , Y. Hu , M. Shi , X. Lu , C. Qin , C. Li , M. Ye , *Chem. Mater.,* **21** , 3514 (2009)

[8]. D. Li, M. B. Müller, S. Gilje, R. B. Kaner, G. G. Wallace, *Nature Nanotechnology* **3**, 101-105 (2008).

[9]. S. Stankovich, D. A. Dikin, R. D. Piner, K. A. Kohlhaas, A. Kleinhammes, Y. Jia *et al.*, *Carbon* **45**, 1558–1565 (2007).

[10]. S. Stankovich, R. D. Piner, X. Chen, N. Wu, S. B. T. Nguyen, R. S. Ruoff, *Journal of Materials Chemistry* **2**, 155-158 (2006).

[11]. F. Xiaobin, P. Wenchao, L. Yang, L. Xianyu, W. Shulan, Z. Guoliang *et al.*, *Advanced Materials* **20**, 4490-4493 (2008).

[12]. M. F. El-Kady, V. Strong, S. Dubin, R. B. Kaner, *Science* **335**, 1326-1330 (2012).

[13]. V. Strong, S. Dubin, M. F. El-Kady, A. Lech, Y. Wang, B. H. Weiller *et al.*, *ACS nano* **6**, 1395-1403 (2012).

[14]. M. F. Elkady, R. B. Kaner, *Acs Nano* **8**, 8725-8729 (2014).

[15]. Y. L. Zhang, L. Guo, H. Xia, Q. D. Chen, J. Feng, H. B. Sun, *Advanced Optical Materials* **2**, 10-28 (2014).

[16]. L. Guo, H.-B. Jiang, R.-Q. Shao, Y.-L. Zhang, S.-Y. Xie, J.-N. Wang *et al.*, *Carbon* **50**, 1667-1673 (2012).

[17]. Z. Fan, R. Kanchanapally, P. C. Ray, *Journal of Physical Chemistry Letters* **4**, 3813-3818 (2013).

[18]. J. Xu, C. Wang, Z. Rong, R. Xiao, X. A. Cheng, *Rsc Advances* **5**, 62101-62109 (2015).

[19]. G. Giallongo, R. Pilot, C. Durante, G. A. Rizzi, R. Signorini, R. Bozio *et al.*, *Plasmonics* **6**, 725-733 (2011).

[20]. R. Zhang, B. B. Xu, X. Q. Liu, Y. L. Zhang, Y. Xu, Q. D. Chen *et al.*, *Chemical Communications* **48**, 5913-5915 (2012).

[21]. X. Bin-Bin, Z. Yong-Lai, Z. Wen-Yi, L. Xue-Qing, W. Jian-Nan, Z. Xu-Lin *et al.*, *Advanced Optical Materials* **1**, 56-60 (2013).

[22]. F. Lin, L. Shuhong, L. Yingshun, L. Huanjun, Z. Lingjuan, Z. Jin *et al.*, *ChemInform* **34**, (2003).

[23]. E. Galopin, J. Barbillat, Y. Coffinier, S. Szunerits, G. Patriarche, R. Boukherroub, *Acs Applied Materials & Interfaces* **1**, 1396-1403 (2009).

[24]. J. A. Huang, Y. Q. Zhao, X. J. Zhang, L. F. He, T. L. Wong, Y. S. Chui *et al.*, *Nano Letters* **13**, 5039-5045 (2013).

[25]. J. Fang, Y. Yi, B. Ding, X. Song, *Applied Physics Letters* **92**, 131115-131115-131113 (2008).

[26]. T. A. Laurence, G. B. Braun, N. O. Reich, M. Moskovits, *Nano Letters* **12**, 2912-2917 (2012).

[27]. W. R. C. Somerville, B. Auguie, E. C. L. Ru, in *Nanotechnology (IEEE-NANO), 2012 12th IEEE Conference on*. (2012), pp. 1 - 4.

[28]. L. Gunnarsson, E. J. Bjerneld, H. Xu, S. Petronis, B. Kasemo, M. Käll, *Applied Physics Letters* **78**, 802-804 (2001).

[29]. B. Michael, S. Vladimir, ouml, s. Ulrich, S. Thomas, Andr *et al.*, *Small* **4**, 398-404 (2008).

Chapter 4.

Raman study on Ag coated laser-structured black silicon

In this chapter, AgNPs decorated laser-structured black silicon (Ag-black silicon) is introduced. Compared with other methods (such as RIE), laser fabrication is much easier to carry out, designable and convenient for large area patterning. When studied as a Raman substrate, they effectively enhanced the Raman signal and realized a detection limit about 10^{-8} M. Specially, these Ag-black silicon structures are manipulated in a microfluidic channel, they realized in-situ enhanced Raman monitoring of on-chip chemical interactions.

4.1 Design and fabrication of Ag-black silicon structures

In recent years, black silicon becomes a famous material, which can be applied in the areas of photodetectors [1-3], solar cells [4-6], sensors [7] and terahertz applications [8-10]. For it has many remarkable properties, such as large absorption range and high specific surface area [11-15]. When the micro/nano-roughened surface is coated with metal nanoparticles, black silicon could be utilized for various other applications, such as surface-enhanced Raman scattering (SERS) sensors [16-18]. However, in the previous work, the black silicon structures were fabricated through relative complicated methods, such as reactive ion etching (RIE) or oxygen plasma etching. These methods are not easy to carry out, and their performances on structuring black silicon surface are not stable. Thus, to overcome these obstacles, laser patterning method is introduced for the black silicon fabrication.

Introduction of black silicon

Basically speaking, black silicon is semiconductor material with a corn-shaped surface structure, where the needles (or pointed corns) are made of single-crystal silicon. Thus normally the black silicon surface presents very low reflectivity and relative high absorption in the visible and infrared light range. Interestingly, black silicon was discovered since the early 1980's, when researchers found an unwanted side effect of reactive ion etching (RIE) [19]. Similar structures could also be formed by other methods, such as dry etching, laser ablation, electrochemical etching and laser-assisted chemical etching. Particularly, the black silicon fabrication by femtosecond laser treatment is effective, which is developed by Eric Mazur's group at Harvard University [20, 21]. Figure 4.1(a) shows an SEM image of black silicon fabricated by Mazur's group [20].

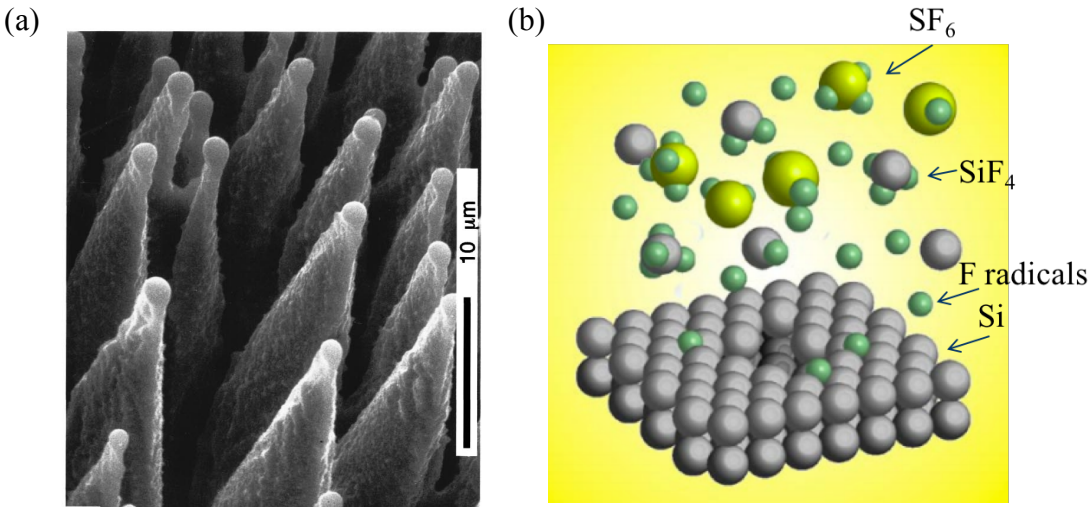

Figure 4.1 Sharp conical spikes produced on Si (100) femtosecond laser viewed (a) 45° from the surface normal. (b) Illustration of black silicon formation mechanism. [20]

The morphology of black silicon usually appears needle-shaped surface structure; while Figure 4.1 (b) illustrates the mechanisms for laser-fabricated black silicon structures formation. They are formed through laser ablation and laser assist chemical etching (details are still under debating). The silicon wafer was usually placed in a SF_6 filled removable chamber, when illuminated by the focused femtosecond laser, due to the strong pulse laser intensity, the silicon would first absorb laser energy and soon be melted and ablated. By the same time, the SF_6 air in the focus volume would be ionized to chemical active F^+ (and S^{6-}). The F^+ will etch the Si surface to form pointed-corn structures [21, 22].

As shown in the image, the black silicon needles have a height about 10 μm and a diameter around 1 μm. The arrangement is relatively uniform. The main feature of this black silicon structure is an increased absorption in visible range light, accordingly the reflectivity on the black silicon surface decreased from 20–30% (quasi-normal incidence) to about 5%. This is because of the formation of the needle-shaped structures, where there is no sharp interface, but a continuous refractive index change, this greatly reduces Fresnel reflection [22]. Actually, most of the applications of black silicon are based on this property.

Femtosecond laser direct wring for black silicon fabrication

In this research, we used femtosecond laser direct writing (FsLDW) method for the black silicon fabrication, which has many remarkble advantages, such as nano-precision, mask-free, and noncontact [24-36]. The optical setup is illustrate by Figure 4.2. The FsLDW process was conducted in a sealed chamber filled with SF_6 at a pressure of 0.07-Mpa. The 800-nm femtosecond laser pulses used here were generated by a Ti:sapphire regenerative amplifier laser system (Spectra Physics). The laser pulse duration was 100 fs and the repetition rate was 1 KHz [37-44]. The laser power was 600 mW, and the scanning speed was 1 mm/s. The desired pattern was completed by manipulating the position of the substrate stage through PC controlled piezoelectric transducer.

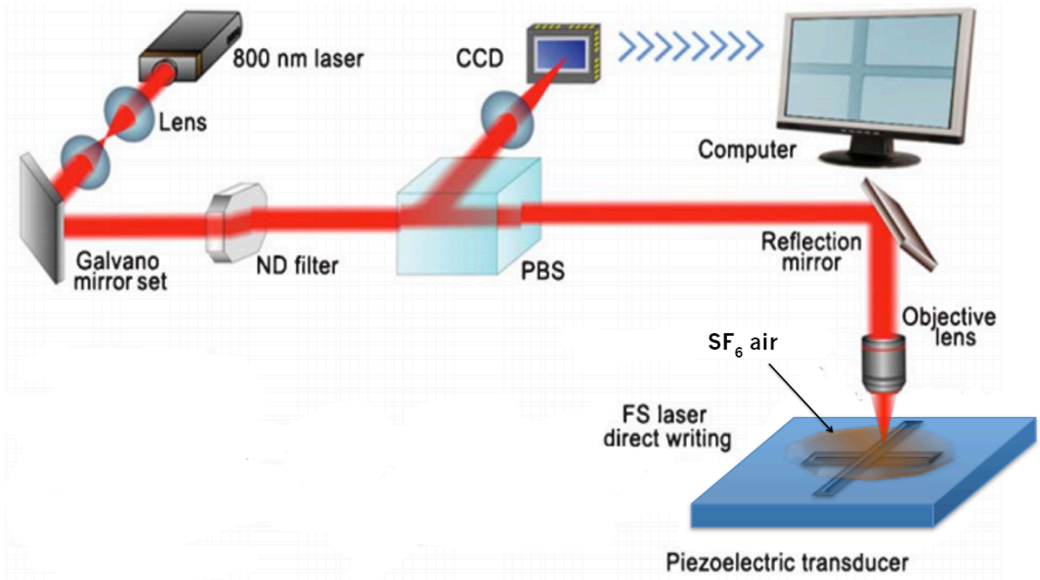

Figure 4.2 Schematic illustration of optical setup for black silicon preparation. [37]

The scheme of the whole process of Ag-black silicon structures fabrication is briefly illustrated in Figure 4.3.

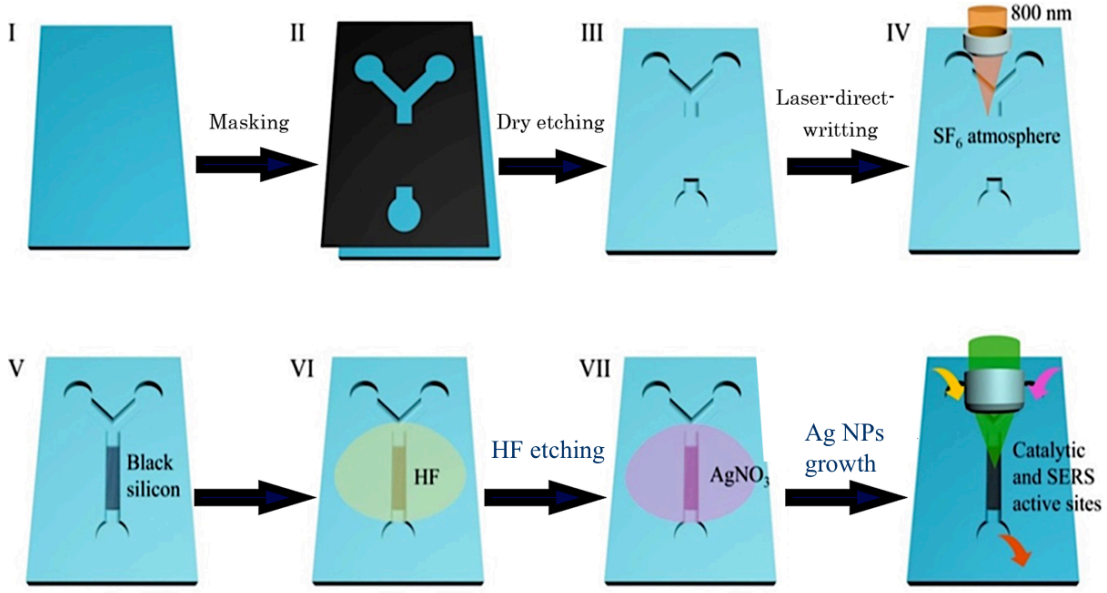

Figure 4.3 Schematic illustration of the whole Ag-black silicon fabrication process. (I~III) Microfluidic chip fabrication on Si wafer by dry etching. (IV~V) black silicon fabrication by laser. (VI) HF treatment on black silicon. (VII) AgNPs growth on black silicon. (VIII) Catalytic reaction and SERS detection on Ag-black silicon substrate.

As illustrated in Figure 4.3, from step I to step III, a "Y" shape microfluidic channel with a 1-cm long non-etched part was first fabricated on a silicon wafer using dry etching [27]. The channel was about 200 μm in width and 20μm in depth. Then VI -V shows the black silicon arrays patterning process on the non-etched part by FsLDW. The FsLDW process was conducted in a sealed chamber filled with SF_6. Before the AgNPs growth, the black silicon surface was treated by HF solution to remove the oxide layer (step VI), and then immersed into $AgNO_3$ solution. The silver ions were reduced into silver and attached on the surface of black silicon as shown in VII. Finally, catalytic reaction and SERS detection are carried out on Ag-black silicon area as shown in step VIII. The reduction of p-nitrosophenol (pNP) to p-aminophenol (pAP) by $NaBH_4$ was chosen as a model reaction for both on chip catalytic test and in-situ SERS detection[35-36]. $NaBH_4$ and pNP solution were injected into two branches of the ''Y'' shape channel, respectively. The reduction started when the two reactants mixed together in the Ag-black silicon area. In-situ SERS detection was then carried out, which could evaluate the reduction process of pNP to pAP.

Characterization of black silicon nano-corns

After the FsLDW process, scanning electron microscope (SEM) was utilized to image the morphology of the black silicon structures. The SEM images and energy dispersive spectrometer (EDS) spectra were taken by field-emission scanning electron microscope/energy-dispersive spectrometer (FESEM/EDS, JSM-7500F, JEOL, Japan). The details are shown in Figure 4.4 (a-b), the surface presents a quasi-ordered arrangement of micro-pointed cones with a height about 18 μm and a diameter of less than 1μm. When utilized as catalysts template, these micro pointed cones would greatly increase the effective contact area between the reactants and catalysts. When combined with metal-NPs, the nanoscale-roughened surface would help generating localized surface plasmon polaritons (LSPPs) to enhance electromagnetic field.

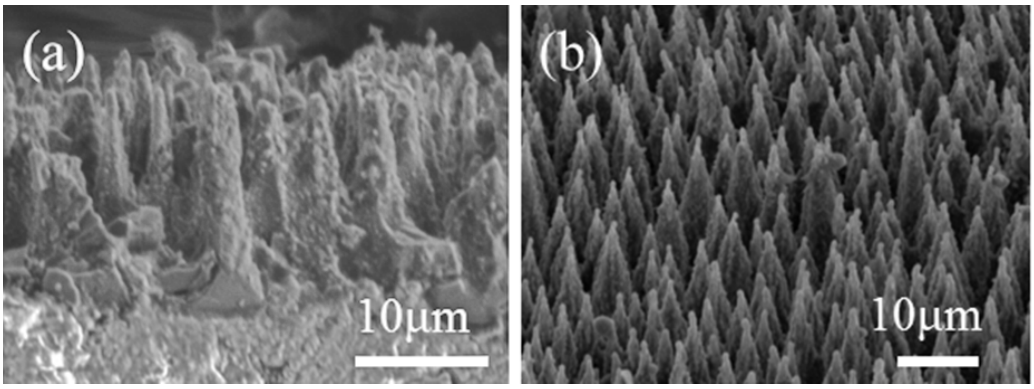

Figure 4.4 SEM images of the BS with (a) side view and (b) oblique view, respectively.

Silver nanoparticles grown on Black silicon

Metal decorated black silicon system have showed great potential as SERS substrate. Till now most of metal-black silicon systems were prepared by physical methods such as magnetron sputtering or evaporation [45-47]. In this research, for the first time to our knowledge, a chemical growth method to grow silver NPs (AgNPs) on black silicon on a microfluidic chip is reported. Compared with earlier works, the chemical growth approach here has important advantages, including site-selectivity and probable higher stability via stronger affinity.

After prepared by FsDLW treatment, the black silicon surface was treated by 2% HF solution for 5 min to remove the oxide layer and to passivate it by hydrogen. This process would greatly increase the reducing reactivity of black silicon surface [48, 49]. Then, the wafer was immersed into a silver nitrate solution ($AgNO_3$) to prepare the Ag-black silicon micro/nano-structures(Figure 4.3 VI).. The silver ions were reduced into silver and attached on the surface of black silicon (Figure 4.3 VII). The parameters influencing the growth of AgNPs were studied.

The morphology of AgNPs on black silicon protrusions was studied by SEM (Figure 4.5).

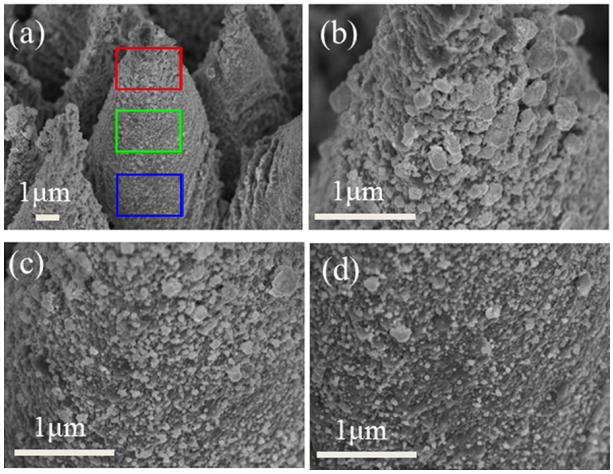

Figure 4.5 (a) SEM image of the AgNPs on the BS protrusions. (b), (c), (d) Enlarged SEM images of AgNPs on the area marked by red, green and blue square in (a).

As shown in Figure 4.5, what is interesting is that AgNPs on different parts of a single black silicon pointed-corn show different sizes and shapes. The AgNPs on the top (Figure 4.5 (b)) were larger and distributed more densely. The size of the AgNPs was about 200nm, 50nm and 10nm at the top, middle and bottom position of the protrusion respectively (Figure 4.5 (b~d)). The reason can be concluded as that the chemical potential on the top position was larger than that of the other part, so when immerged in $AgNO_3$ solution, the top-part surface would be more active and reduce more AgNPs.

It is well known that high temperature will promote the growth of the AgNPs. In order to get an optimized temperature for AgNPs synthesis, the AgNPs growth under 4 different temperatures was examined by SEM, as shown in Figure 4.6 (a~d). At 15^{o}C, the size of the nanoparticles is relatively small (1~2 nm). As for the temperatures of 25^{o}C and 50^{o}C, the nanoparticles size increase to 20nm and 50nm, respectively. When the temperature reaches 75^{o}C, the AgNPs become larger than 100 nm and the shape become irregular rather than spherical. Because the larger and irregular shape AgNPs are not beneficial for catalysis, we chose the room temperature (25^{o}C) as the condition for the AgNPs growth.

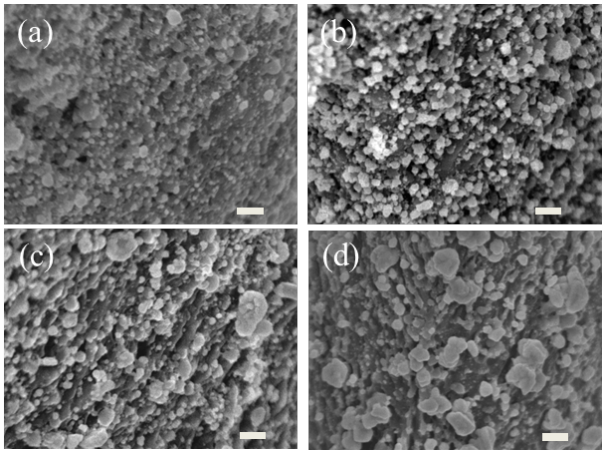

Figure 4.6 SEM images of the AgNPs grown under (a) 15℃,(b) 25℃, (c) 50℃,(d) 75℃. The scale bars indicate 100nm.

Another important factor that affects the growth of AgNPs is the solution concentration. In this section, 4 different concentrations of AgNO3 solution were used to to get an proper one for the AgNPs growth. As shown in Figure 4.7 (a~d), when AgNO3 concentration was down to 0.001 M, the size of the nanoparticles was rather small (~1nm), and they spread over the surface of the black silicon sparsely. As the solution concentration increased to 0.01 M, 0.1 M and 1 M , both the nanoparticles size and density became larger. However, when the concentration reached 1M (Figure 4.7 (d)), the nanoparticles became too large and presented more like block-shape with fewer gaps, it was obviously not suitable for both catalysis and LSPPs generation. Hence, we chose 0.1 M as the best concentration of AgNO3 solution for AgNPs sythesis.

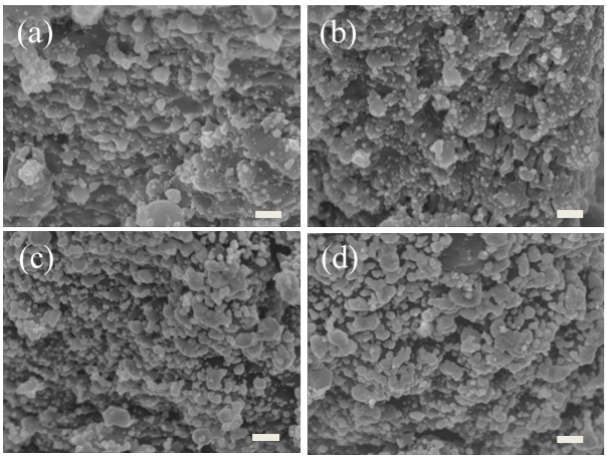

Figure 4.7 SEM images of AgNPs grew by (a). 0.001M, (b) 0.01M, (c) 0.1M, (d) 1M AgNO3 solution. The scale bars indicate 100nm.

To confirm the optimized conditions (25°C, 0.1M $AgNO_3$ solution) for AgNPs growth, besides SEM, EDS was also carried out. Figure 4.8 shows EDS spectra of the Ag-black silicon structures. The distinct energy peak of Ag can be observed under various temperature (Figure 4.8 (a)) and different $AgNO_3$ solution concentration (Figure 4.8 (b)), which indicates the existence of the silver element on the black silicon surface. As illustrated in the insets of Figure 6a and 6b, the silver content increases with the reaction temperature and the $AgNO_3$ solution concentration, which is consistent in agreement with the previous discussion.

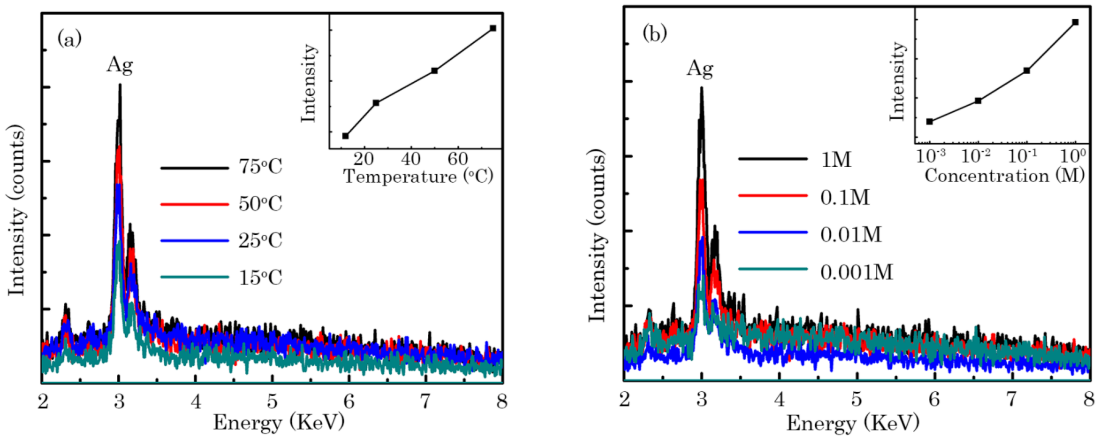

Figure 4.8 EDS spectra of the Ag-BS (a) under different reaction temperatures, inset shows the peak intensity versus temperature; and (b) with different $AgNO_3$ solution concentration, inset shows the peak intensity versus concentration.

4.2 SERS characterization of Ag-black silicon structures

By using R6G as a probe molecule, the SERS activity of the silver-black silicon substrate was studied. The Raman spectrum of the R6G with concentrations of 10^{-8} M is shown in Figure 4.9.

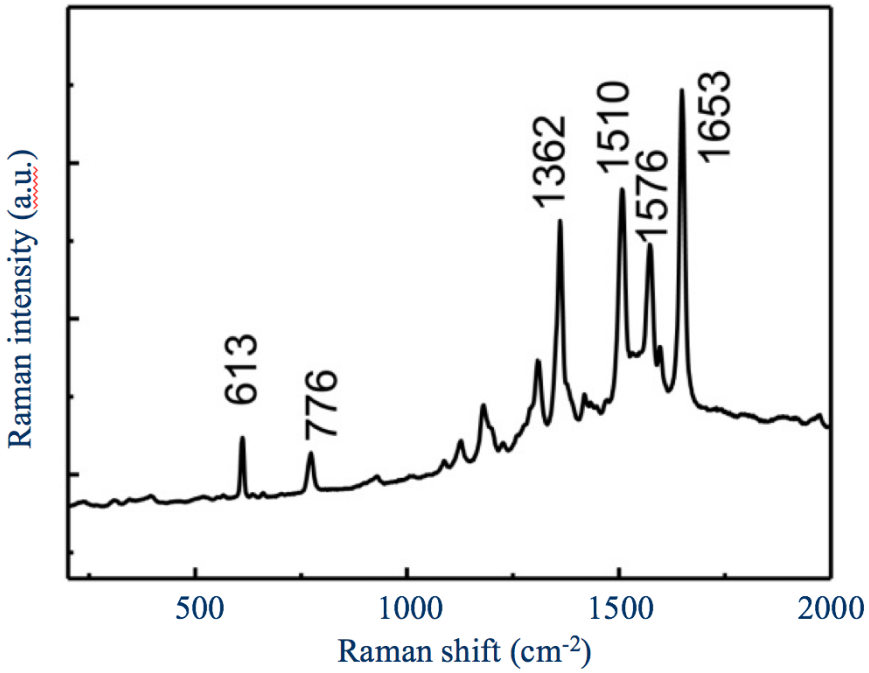

Figure 4.9 SERS of R6G with the concentrations of 10^{-8}M on Ag-black silicon structures.

The distinct peaks (613, 776, 1362, 1510, 1576, 1653 cm^{-1}) [52] with high S/N ratio are clearly observed, even for the concentration of 10^{-8} M. It indicated that the Ag-black silicon substrate has large Raman enhancement. The strong SERS enhancement can be explained by the dramatically enhanced electromagnetic field on the rough distributed AgNPs on the black silicon substrate [7]. Importantly, the catalytic reactors themselves (hierarchically micro/nano-structurised Ag-black silicon composite devices) worked as the SERS sensors for chemical reaction and analysis in the same time, which might be of great help to improve the chip integration.

The on chip catalytic reaction and in-situ SERS detection process is illustrated in Figure 4.10. The reduction of pNP to pAP by $NaBH_4$ was chosen as a model reaction for both on chip catalytic test and in-situ SERS detection [50, 51]. pAP is a famous analytical reagent, and also widely used as intermediates for synthesizing pharmaceutical, dyes and other fine chemicals. It is usually produced from pNP reduction. Thus an in-situ monitoring is of great value for understanding the dynamic chemical reaction process.

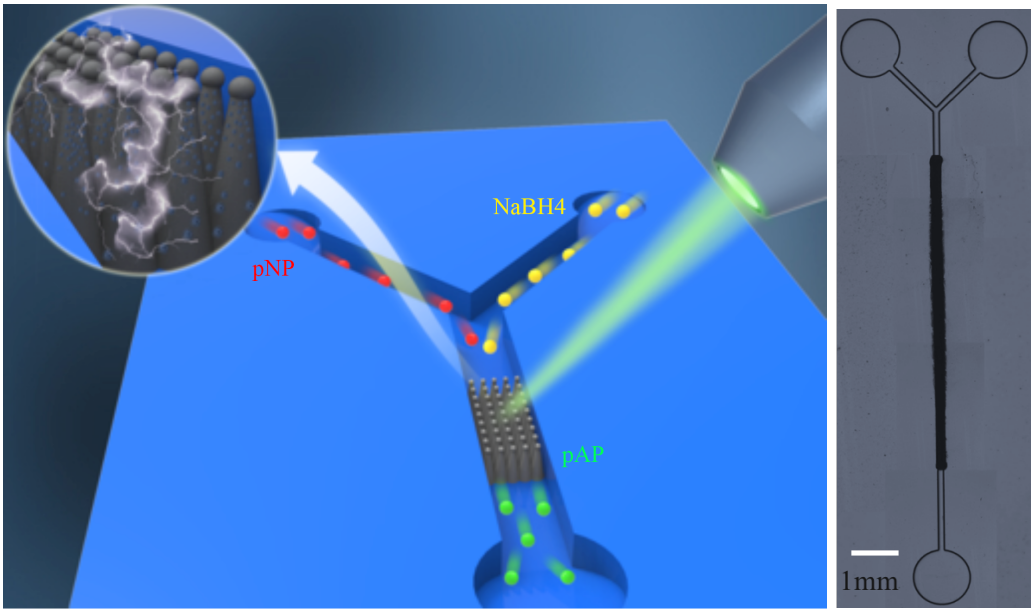

Figure 4.10 Scheme of on chip catalytic reaction and in-situ SERS detection (left) and real photo of micro channels on Si chip (right).

As details, The $NaBH_4$ and pNP were injected into two branches of the ‘‘Y’’ shape channel, respectively. The reduction reaction started when the two reactants mixed together in the Ag-black silicon structures area. In-situ SERS detection was then carried out, which could evaluate the reduction process of pNP to pAP. The Raman spectra were recorded on a LabRAM HR Evolution (from Horiba scientific) equipped with a He-Ne laser at 633 nm as excitation source, the laser power was about 1mW, and the average spot size was 1 μm in diameter. The Raman spectra are shown in Figure 4.11.

The black and red curves in Figure 4.11 represent the SERS spectra of pNP and pAP, taken before and after the catalytic reaction of pNP reduced to pAP, respectively. The Raman mode at 240 cm^{-1} in SERS spectrum before reaction is the peak of nitro bonded to the benzene ring in

pNP molecule; while after the reaction, two distinct Raman modes at 1275 cm^{-1} and 1327 cm^{-1} were clearly observed, which represented the peak of amino bonded to the benzene ring in pAP molecule (see inset of Figure 4.11). Judging by the Raman spectra changes, it is easy to monitor the chemical reaction process. Here the black silicon protrusions helped accomplishing the Ag nanoparticles packed with high surface area, which made them good candidate as catalytic

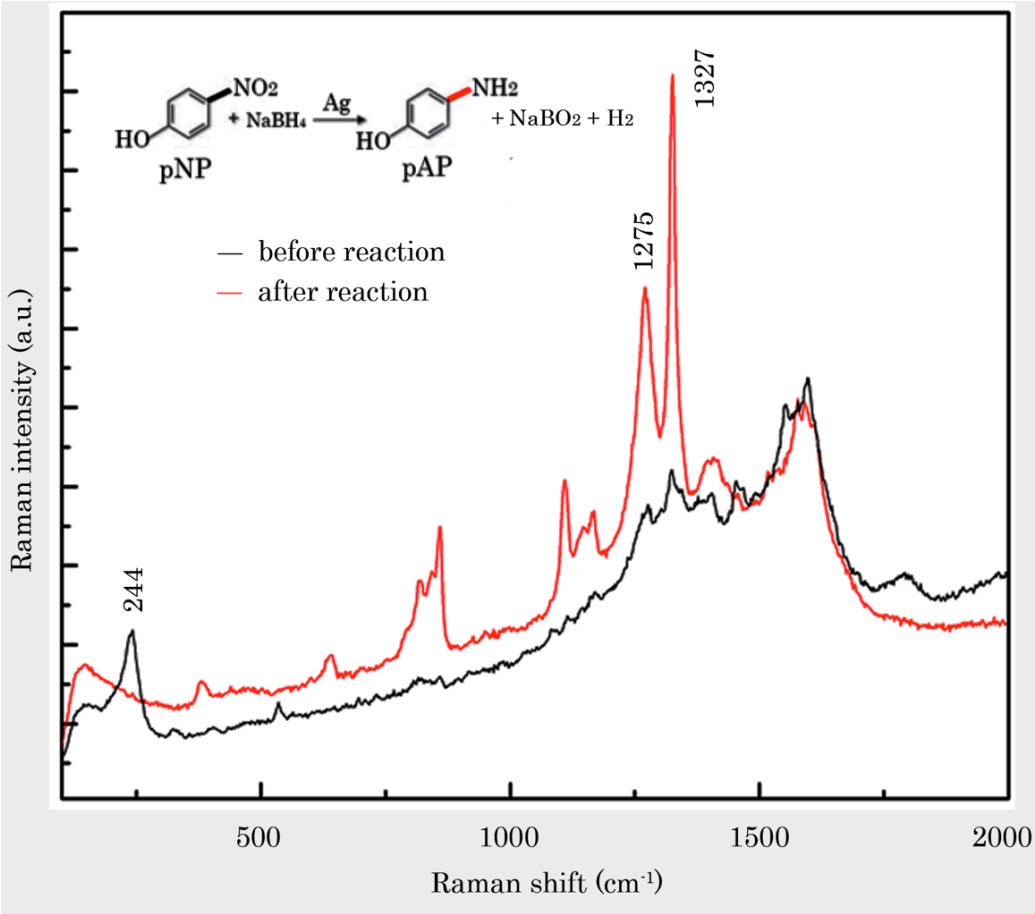

Figure 4.11 SERS spectra taken before (black curve) and after (red curve) the catalytic reaction of pNP to pAP. Inset illustrates the chemical reaction process.

active sites. Also the Ag-black silicon substrate presents its potential for in-situ SERS detection.

Sammary

In this chapter, I introduced a novel micro/nano-structured Ag-black silicon composite devices, which are in-situ constructed and integrated in microfluidic chip. This hierarchical structure simultaneously contribute for catalytic reaction and SERS-based monitoring. black silicon substrate was femtosecond-laser fabricated in the atmosphere of SF_6. For templated-chemical growth of AgNPs , the black silicon was then etched and hydrogenated by HF solution. Considering high Raman enhancement, optimized AgNPs-growth parameters (25°C and 0.1 M $AgNO_3$ solution concentration) were applied to obtain ~20-nm average diameter and dense loading with gaps. When applied for Raman measurement, these Ag-black silicon composite devices showed high sensitivity with a detection limit of 10^{-8} M. While the Ag-black silicon composite structure was applied for catalytic reaction (pNP to pAP) in microfluidics channels, it functioned as in-situ SERS sensors to monitor the reaction processes. As a "generalist" of both catalytic reactors and SERS sensors, the hierarchically micro/nano-structurised Ag-black silicon composite devices here might open new opportunities for various applications like highly integrated chemical synthesis and analysis, and biomedical sensing and diagnosis.

References

[1]. M. Steglich, M. Zilk, A. Bingel, C. Patzig, T. Kasebier, F. Schrempel *et al.*, *Journal of Applied Physics* **114**, 183102-183102-183108 (2013).

[2]. S. Koynov, M. S. Brt, M. Stutzmann, *physica status solidi (RRL) - Rapid Research Letters* **1**, R53-R55 (2007).

[3]. S. Koynov, M. S. Brandt, M. Stutzmann, *Applied Physics Letters* **88**, 203107 - 203107-203103 (2006).

[4]. X. Liu, P. R. Coxon, M. Peters, B. Hoex, J. M. Cole, D. J. Fray, *Energy & Environmental Science* **7**, 3223-3263 (2014).

[5]. Y. Xia, B. Liu, J. Liu, Z. Shen, C. Li, *Solar Energy* **85**, 1574-1578 (2011).

[6]. W.-C. Wang, C.-W. Lin, H.-J. Chen, C.-W. Chang, J.-J. Huang, M.-J. Yang *et al.*, *ACS applied materials & interfaces* **5**, 9752-9759 (2013).

[7]. P. Hoyer, M. Theuer, R. Beigang, E. B. Kley, *Applied Physics Letters* **93**, 091106-091106-091103 (2008).

[8]. H. P. Porte, D. Turchinovich, P. U. Jepsen, S. Persheyev, Y. Fan, M. J. Rose, in *Infrared Millimeter and Terahertz Waves (IRMMW-THz), 2010 35th International Conference on*. (2010), pp. 1 - 3.

[9]. Z. Xiao, C. Feng, P. C. H. Chan, I. M. Hsing, in *Solid-State Sensors, Actuators and Microsystems Conference, 2007. TRANSDUCERS 2007. International*. (2007), pp. 89-92.

[10]. Y. Murakami, T. Takeuchi, K. Yokoyama, E. Tamiya, I. Karube, M. Suda *et al.*, *Analytical Chemistry* **65**, 2731-2735 (1993).

[11]. T.-H. Her, R. J. Finlay, C. Wu, S. Deliwala, E. Mazur, Appl. Phys. Lett. 73, 1673-1675 (1998).

[12]. T. H. Her, R. J. Finlay, C. Wu, E. Mazur, Appl. Phys. A-Mater. 70, 383-385 (2000).

[13]. Z. Fekete, A.C. Horvath, Z. Berces, A. Pongracz, *Sensors & Actuators A Physical* **216**, 277–286 (2014).

[14]. M. Hong, G. D. Yuan, Y. Peng, H. Y. Chen, Y. Zhang, Z. Q. Liu *et al.*, *Applied Physics Letters* **104**, 253902-253902-253905 (2014).

[15]. J. Yang, F. Luo, T. S. Kao, X. Li, G. W. Ho, J. Teng *et al.*, *Light Science & Applications* **3**, e185 (2014).

[16]. Y. Chen, G. Kang, A. Shah, V. Pale, Y. Tian, Z. Sun *et al.*, *Advanced Materials Interfaces* **1**, 1 (2013). 1. I. Talian, K. B. Mogensen, A. Oriňák, D. Kaniansky, J. Hübner, *Journal of Raman Spectroscopy* **40**, 982-986 (2009).

[17]. G. Gervinskas, G. Seniutinas, J. S. Hartley, S. Kandasamy, P. R. Stoddart, N. F. Fahim *et al.*, *Annalen der Physik* **525**, 907-914 (2013).

[18]. H. Jansen, D. M. Boer, R. Legtenberg, M. Elwenspoek, *Journal of Micromechanics & Microengineering* **5**, 115-120 (1995).

[19]. T.-H. Her, R. J. Finlay, C. Wu, S. Deliwala, E. Mazur, *Applied Physics Letters* **73**, 1673 (1998).

[20]. T.-H. Her, Harvard University Cambridge, Massachusetts, (1998).

[21]. T. C. Choy, *Effective medium theory: principles and applications*. (Oxford University Press, 1999).

[22]. Y. Xu, H. B. Sun, J. Y. Ye, S. Matsuo, H. Misawa, J Opt. Soc. Am. **18,** 1084 (2001).

[23]. Y.-L. Sun, W.-F. Dong, L.-G. Niu, T. Jiang, D.-X. Liu, L. Zhang *et al.*, *Light Sci Appl* **3**, e129 (2014).

[24]. R. Kammel, R. Ackermann, J. Thomas, J. Gotte, S. Skupin, A. Tunnermann *et al.*, *Light Sci Appl* **3**, e169 (2014).

[25]. K. Sugioka, Y. Cheng, *Light Sci Appl* **3**, e149 (2014).

[26]. R. Zhang, C. Lu, X. Xiao, Y. Luo, Y. Xu, *Chem. J Chinese Universities* **35**, 471-475 (2014).

[27]. R. Zhang, C. Lu, X.-Z. Xiao, Y. Luo, Y. He, Y. Xu, *Acta Physica Sinica* **63**, (2014).

[28]. S. Kawata, H. B. Sun, T. Tanaka, K. Takada, *Nature* **412**, 697-698 (2001).

[29]. X. B. Li, X. Q. Liu, X. Lin, D. Han, Z. Zhang, X. D. Han, H. B. Sun, and S. B. Zhang, *Phys*. *Rev*. *Lett*. **107,** 015501 (2011).

[30]. Y. L. Zhang, Q. D. Chen, H. Xia, and H. B. Sun, *Nano Today* **5**, 435 (2010).

[31]. X. B. Li, X. Q. Liu, X. D. Han, and S. B. Zhang, Phys. *Status Solidi B* **249,** 1861 (2012).

[32]. Y. L. Zhang, L. Guo, S. Wei, Y. Y. He, H. Xia, Q. D. Chen, H.-B. Sun, and F. S. Xiao, *Nano Today* **5,** 15 (2010).

[33]. H. Xia, J. Wang, Y. Tian, Q. D. Chen, X. B. Du, Y. L. Zhang, Y. He and H. B. Sun, *Adv. Mater.* **22**, 3204 (2010*)*.

[34]. Y. L. Sun, W. F. Dong, R. Z. Yang, X. Meng, L. Zhang, Q. D. Chen, H. B. Sun, *Angew. Chem. Int. Ed.* **51***,* 1558 (2012).

[35]. D. Wu, J. Xu, L. G. Niu, S. Z. Wu, K. Midorikawa, and K. Sugioka, *Light Sci*. *Appl*. **4,** e228 (2015).

[36]. Y. He, B.-L. Huang, D.-X. Lu, J. Zhao, B.-B. Xu, R. Zhang *et al.*, *Lab on a Chip* **12**, 3866-3869 (2012).

[37]. L. Wang, Q. D. Chen, R. Yang, B. B. Xu, H. Y. Wang, H. Yang, C. S. Huo, H.-B. Sun, and H. L. Tu, *Appl*. *Phys*. *Lett*. **104**(2014).

[38]. J. H Zhao, C. H. Li, Q. D. Chen, and H. B. Sun, *IEEE Sens*. *J*. **15,** 4259 (2015)..

[39]. C. Chen, Y. S. Yu, R. Yang, L. Wang, J. C. Guo, Q. D. Chen, and H. B. Sun, , IEEE *J. Lightwave Technol*. **29,** 2126 (2011).

[40]. D. Wu, S. Z. Wu, Q. D. Chen, Y. L. Zhang, J. Yao, X. Yao, L. G. Niu, J. N. Wang, L. Jiang, and H. B. Sun, *Adv*. *Mater*. **23,** 545 (2011).

[41]. D. Wu, J. N. Wang, S. Z. Wu, Q. D. Chen, S. Zhao, H. Zhang, H. B. Sun, and L. Jiang, *Adv. Funct. Mater.* **21,** 2927 (2011).

[42]. L. Guo, Y. L. Zhang, R. Q. Shao, S. Y. Xie, J. N. Wang, X. B. Li, F. Jiang, H.-B. Jiang, Q.-D. Chen, T. Zhang and H.-B. Sun, *Carbon* **50,** 1667 (2012).

[43]. R. Yang, Y. S. Yu, C. Chen, Q. D. Chen, and H. B. Sun, *Opt*. *Lett.* **36,** 3879 (2011).

[44]. M. S. Schmidt, J. Hubner and A. Boisen, *Adv*. *Mater*. **24,** OP11 (2012).

[45]. H. Mao, W. Wu, D. She, G. Sun, P. Lv and J. Xu, *Small* **10,** 127 (2014).

[46]. P. Zhang, S. Li, C. Liu, X. Wei, Z. Wu, Y. Jiang and Z. Chen, *Nanoscale Res*. *Lett*. **9，** 519 (2014).

[47]. X. H. Sun, R. Sammynaiken, S. J. Naftel, Y. H. Tang, P. Zhang, P.-S. Kim, T. K. Sham, X. H. Fan, Y.-F. Zhang, C. S. Lee, S. T. Lee, N. B. Wong, Y.-F. Hu and K. H. Tan, *Chem. Mater.* **14,** 2519 (2012).

[48]. X. H. Sun, Y. H. Tang, P. Zhang, S. J. Naftel, R. Sammynaiken, T. K. Sham, H. Y. Peng, Y.-F. Zhang, N. B Wong, and S. T. Lee, *J Appl. Phys.* **90**(12), 6379 (2001).

[49]. B. B. Xu, R. Zhang, X. Q. Liu, H. Wang, Y. L. Zhang, H. B. Jiang, L. Wang, Z. C. Ma, J. F. Ku, F. S. Xiao, H. B. Sun, *Chem. Commun.* **48,** 1680 (2012).

[50]. B. B. Xu, Z. C. Ma, L. Wang, R. Zhang, L. G. Niu, Z. Yang, Y. L. Zhang, W. H. Zheng, B. Zhao, Y. Xu, Q. D. Chen, H. Xia, and H. B. Sun, *Lab on a Chip* **11,** 3347 (2011).

[51]. R. Zhang, B.-B. Xu, X.-Q. Liu, Y.-L. Zhang, Y. Xu, Q.-D. Chen, and H.-B. Sun, *Chem. Commun.* **48,** 5913 (2012).

Chapter 5.

Raman study of FIB-structured ZnO

In this chapter, FIB-designed nanoscale structures on ZnO surface are introduced. These structures are formed by Ga ions doping in the ZnO surface laser with less morphology change, which are similar to the structures in integrated circuits (IC). Thus it is difficult for normal methods (such as AFM, SEM) to characterize. Using Raman spectroscopy, the ZnO lattice changes on the doped area was detected through comparing Raman modes differences. The distribution of the doped structures was also achieved through Raman imaging. Through this work, Raman showed great potential for characterizing ion doped semiconductors. As a future expectation, combined with a metallic tip, though tip enhancing process, Raman technology will realize nanoscale analyze of the tiny structures in IC. It will greatly improve the technology in IC industry.

5.1 Nanoscale Ga ions doped ZnO designed by FIB

Now, our life is greatly improved by the development of the microelectronic techniques, such as PC, cell phone. And this useful technology is still under developing. The two main directions are: high integration and small feature size. The feature size has already reached 14nm by the year 2014, and is estimated to reach even smaller in the future. So there is a need to image and analyze such tiny structures, which can promote its evolvement [1].

As we know, the feature size of microelectronic devices is a description of the minimum size that can be patterned by doping. So the common used scanning methods such as AFM or SEM become invalid, because they can only provide topographic variations, but no inner composition and structure changing information. Raman spectroscopy may realize this goal by testing the inner composition and crystal lattice changes [2-3].

As a first step, Nanoscale ion doped semiconductor was prepared by FIB technology. Similar to the doping process in IC industries, Ga ions were doped into surface layer of ZnO single crystal. The chosen of Ga and ZnO material chosen here was based on the consideration of simple preparation and convinent for Raman measurement. The FIB system I used is FB2200 from Hitachi Company, it can realize nanoscale doping with a 10nm resolution. The real photo of the system is shown in Figure 5.1

Figure 5.1 Optical image of FB2200 (Hitachi) FIB system

FIB fabrication parameters I used are as follows:

Voltage: 20kV, current:10pA , time:6s/line, length: 30um, dose: 6.25×10^{16} cm^{-2}

The accelaration voltage chosen here was for getting shallow doped area and less surface damage. Normally the doping depth is proportional to the doping voltage, for example: for 20kV, the doping depth is in the range of 0~20nm, which is proper for Raman detection. When using low accelaration voltage, the surface damage became large with a large line width. So considering shallow doping depth, narrower line width and less surface damage, 20kev ions is better for my sample fabrication. After the

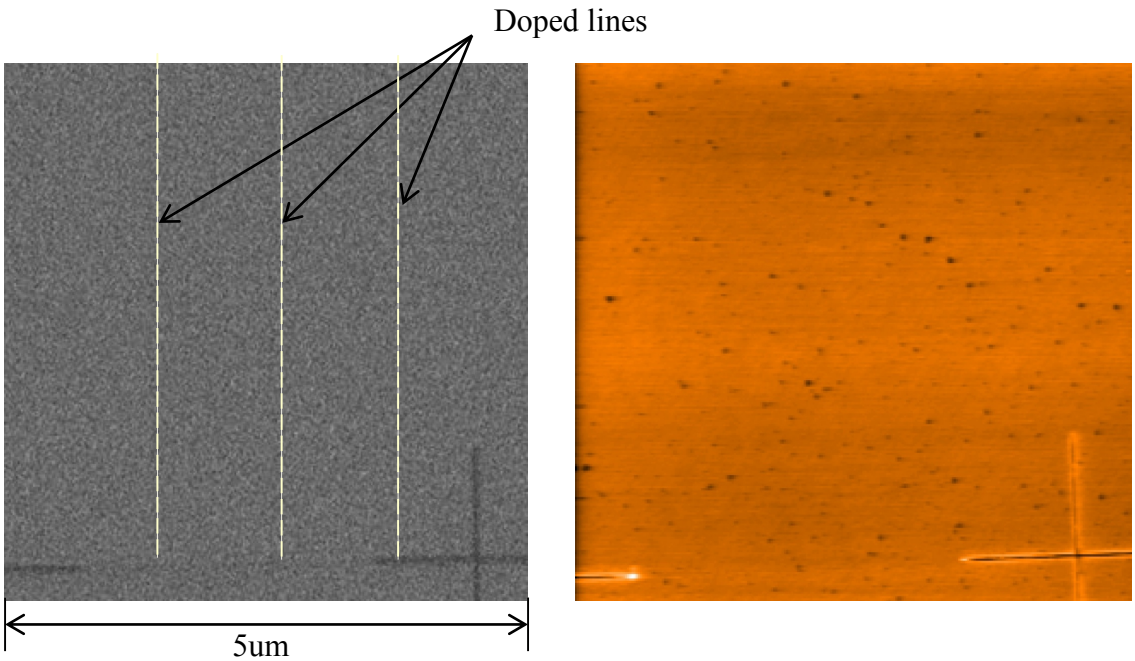

Figure 5.2 SEM image (left) and AFM image (right) of the Ga ions doped nanolines (marked by the white dot lines) on ZnO.

doping process, both AFM and SEM were conducted to characerize the morphology of the doped area. As shown in Figure 5.2, after doping, the surface damage of the doped area is very less. We can even hardly see the 3 nanolines near the cross marks from the AFM and SEM images.

5.2 Micro Raman imaging of nanoscale doped ZnO

The optical setup for Raman mesurement is shown in Figure 5.3, it is transmission mode Raman system, just the doped area was put downwards to get well focus condition (avoid the spherical aberration).

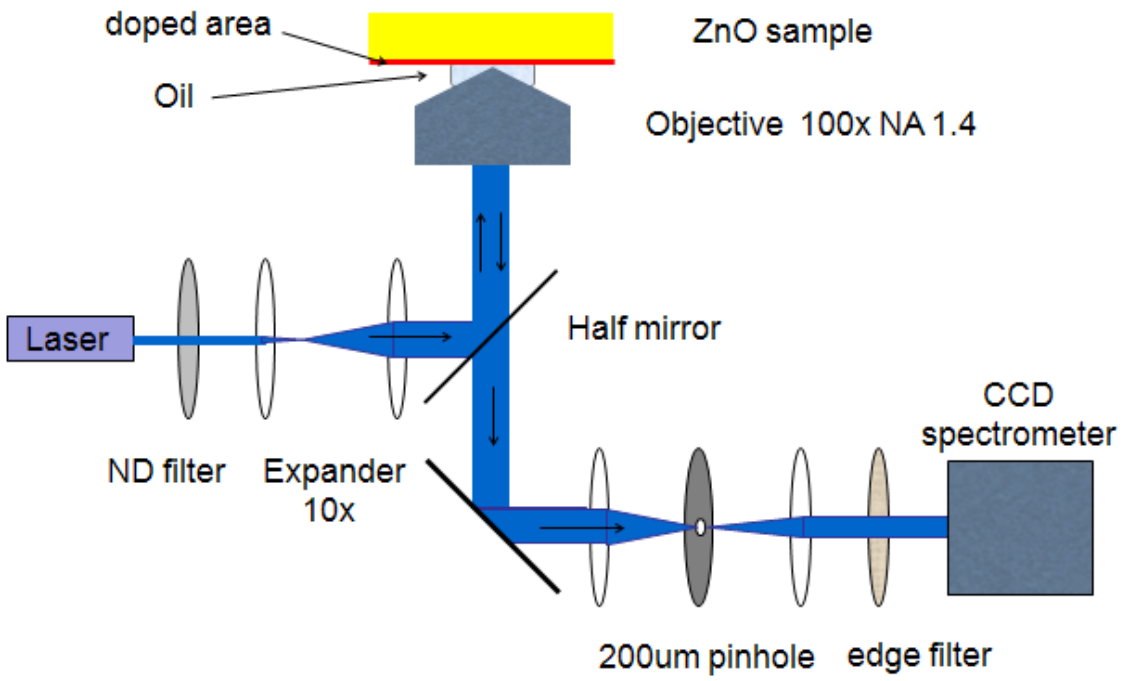

Figure 5.3 Scheme of Raman system.

Raman spectrum of both the Ga doped ZnO and pure ZnO single crystal were measured. The Raman measurement conditions are: 488nm laser, 1.3mw, 10s /frame. The spectra are shown in Figure 5.4. By comparing with the Raman spectrum of pure ZnO single crystal, two abnormal Raman modes were found in the Raman spectrum of the doped area, one is the additional mode at 580cm^{-1}, the other one is a broaden band center around 200cm^{-1}. After checking with some papers, the origin of the 580cm^{-1} mode origins from lattice disorder during the ion implantation [4, 5] and the broadband center at 200cm^{-1} can be assigned to acoustic-phonon branch at the zone boundary [6, 7].

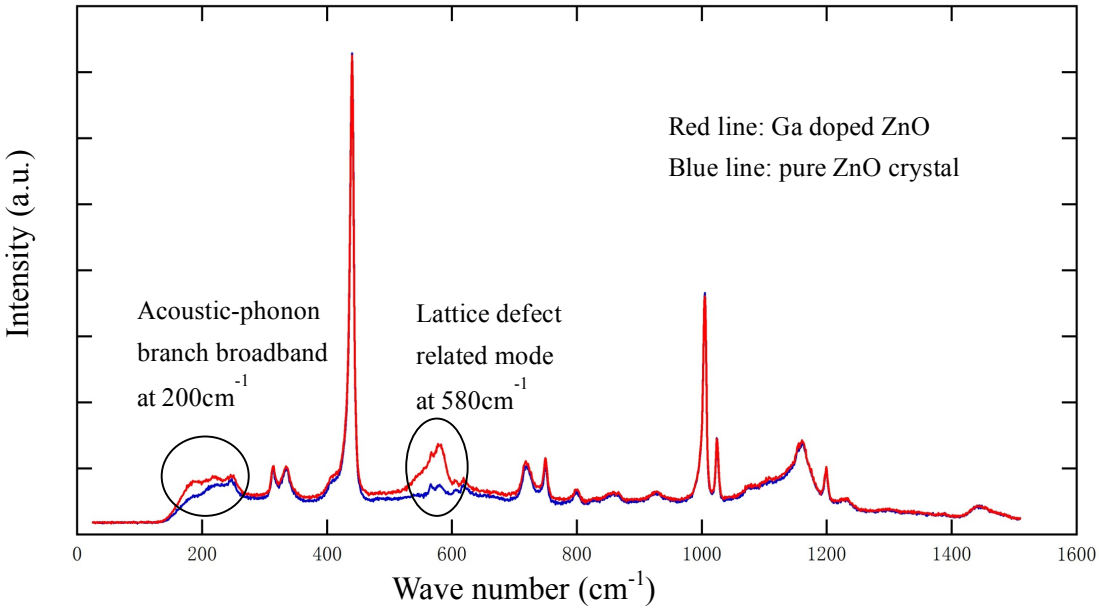

Figure 5.4 Raman spectra of Ga doped ZnO (red) and pure ZnO crystal (blue).

Then by using the abnormal mode at 580cm^{-1}, far field Raman image of the doped lines was taken, see Figure 5.5. For this mode is related to lattice disorder caused by ion implantation, so only the Ga doped area appeared clearly in the Raman image. Comparing with AFM image, the Raman method did show more information than AFM and SEM, and could realize more application in the microelectronic industries. For it is far field Raman image, the resolution is about 300nm that restricted by diffraction limit.

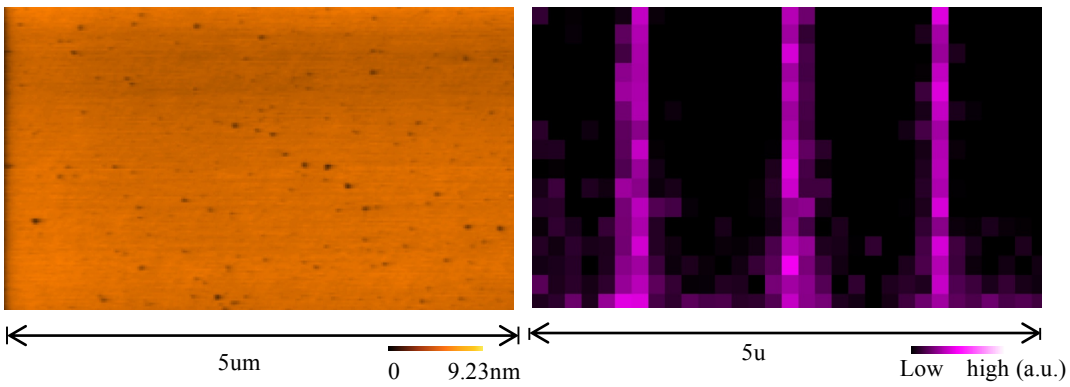

Figure 5.5 AFM image (left) and Raman image (right) of doped nanolines in same area.

5.3 Prospect and future work

The far field Raman result showed its potential for the application in semiconductor world. To characterize the doping property with a nanoscale resolution, TERS technique is crucial needed. As a prospect, by building a TERS system and applying it for the analysis on the nanoscale doped structures on IC chips will hold great interest and value for the development of IC technologies.

For the TERS system, here we should notice that a reflection mode is a better choice, for the IC circuits are based on semiconductors, which are not transparent in visible range; and the design and preparation of metallic tips used for TERS are also very important, which will determine the Raman enhancement.

Sammary

In this chapter, I introduced the fabrication of nanoscale Ga ions doped on ZnO crystals, then using Raman studied the lattice property changes on the doped area. Two different Raman modes were observed which were related to the lattice disorder during the ion implatation process. Using the different Raman mode 580cm^{-1} Raman image of the doped lines was clearly achieved. The Raman result support the future work of applying TERS technology for the nanocale characterization of structures on IC chips, which would be very useful to improve IC design techniques.

References

[1]. Computer Desktop Encyclopedia copyright ©1981-2012 by The Computer Language Company Inc.

[2]. W.X. Sun, Z.X. Shen, *Ultramicroscopy* **94,** 237–244 (2003)

[3]. J. Rinderknecht，A. Shelaev，P. Dorozhkin，L. M. Eng, *Ultramicroscopy* **111,** 1630–1635 (2011)

[4]. P. Y. Peter, M. Cardona, Fundamentals of Semiconductors: Physics and Materials Properties (2010)

[5]. J. Yu, H. Xing, J. Wang, et al., *Solid State Communications* **138,** 502–504 (2006)

[6]. C. Bundesmann, N. Ashkenov, M. Schubert, et al., *Appl. Phys. Lett.* **83**, 1974 (2003)

[7]. J. B. Wang, H. M. Zhong, Z.F. Li, L. Wei, *Appl. Phys. Lett.* **88**, 101913 (2006)

Conclusion

In this dissertation, aimed to solve the challenges that hinder the development of structured surface science towards application in plasmonic and integrated circuits, laser patterning technology and FIB method were introduced to prepare two kinds of structured surface, followed by Raman spectroscopy characterizing and evaluating their performance respectively.

In details, the thesis starts with the introduction of structured surface science, including its fundamentals, applications, developments and challenges. As two powerful surface structuring methods, laser structuring technology and FIB are in detail illustrated.

In the second chapter, Raman spectroscopy for characterizing structured surface is introduced, including its fundamentals, characterization of plasmonic enhancement on metallic structured surfaces and analyzation on ion doped semiconductor surface.

For the research part, the fabrication and characterization of Ag coated laser-structured RGO plasmonic surface were first demonstrated. From Raman studying result, both high Raman enhancement and signal reproducibility were achieved. Using R6G as probe molecule, a LOD of 10^{-10}M and an EF of $2.0x10^{7}$ were got, with a good space reproducibility (RSD~10%) and a good time reproducibility (stable in 3 weeks). All these features are benefit from the uniformity of the RGO stripes template fabricated by TBLI and the well-dispersed AgNPs decorated on the nanoscale RGO layers, also the hydrophobicity of the RGO stripes further boost the enhancement by condensation effect. TBLI fabrication of RGO stripes holds great promise for the development of highly efficient plasmonic structures.

As another type plasmonic structured surface, a composite Ag decorated laser structured-black silicon surface were designed and evaluated by Raman spectroscopy. The merit of this substrate was its multifunction, simultaneously served for catalytic reaction and an effective chemical reaction sensor. This technique not only opens a

door to lab on chip application for SERS, but also provides an idea for lab-on-chip multi-functionalization. The results in chapter 3 and chapter 4 support that laser fabrication method holds great potential to make uniform and high sensitive templates for effective plasmonic structures fabrication. This method could promote SERS toward a powerful and stable standard detection methods in chemical, physical and biological area.

In the last chapter, by Raman study of FIB-structured Ga ions doped ZnO was conducted. Raman detected the lattice property changes and clearly imaged doped lines distributions. This result strongly supports that Raman is capable for the application in IC industries. By Building a TERS system together with metallic tips with high EM enhancement, will open a gate for nanoscale Raman studying of ion doped semiconductors, and improve the technologies in IC industries.

The results presented in this thesis support that Raman hold great potential for analyzing various types of structured surface, and laser and FIB technology are of great capacity for efficient surface structures design and fabrication.

List of publications

Original papers

1. **Zhaoxu Yan,** Chunhao Li, Yang Luo, Jihong Zhao, Hai Yang, Prabhat Verma, and Satoshi Kawata, "Silver hierarchical structures grown on microstructured silicon in chip for microfluidic integrated catalyst and SERS detector," Chin. Opt. Lett., 13, 102401 (2015)
2. **Zhao-Xu Yan,** Yong-Lai Zhang, Xiu-Yan Fu, Hao-Bo Jiang, Yu-Qing Liu, Prabhat Verma, Satoshi Kawata, and Hong-Bo Sun, "Superhydrophobic SERS Substrates Based on Silver Coated Reduced Graphene Oxide Gratings Prepared by Two-Beam Laser Interference," Published online, ACS Appl. Mater. Interfaces, 7, 27059 (2015).

Acknowledgement

It is really a long journey to get my PhD degree! Here I would like to express my sincerely gratefulness to all the professors and friends that strongly supported me and help me. Especially to:

Prof. Satoshi Kawata (Osaka University, LaSIE), who is my supervisor during my doctor course. During every talk and discuss, Prof. Kawata always encourages me to face the problems and try to solve them, which strongly supported me to go forward not only for science, but also an attitude to life.

Prof. Prabhat Verma (Osaka University, NaSpec), who advised me during my doctor course in Japan. Prof. Verma is a logical professor, helped me so lot on every details of my research. I really learnt a lot from him, especially how to think and deal with things scientifically.

Prof. Hong-Bo Sun (Jilin University, LaSuN), who was my master course supervisor. During my later part of PhD course, Prof. Sun advised me and helped me to finally complete my research work. Talking with Prof. Sun always give me strength and courage, no matter how huge the challenges are to face with.

Prof. Yuika Saito (Osaka University, NaSpec) and Prof. Atsushi Taguchi (Osaka University, LaSIE). I always got wonderful idea for solving problems when discussing with Prof. Saito and Prof. Taguchi. Their kindness and knowledge were really impressed me so lot.

Prof. Yong-Lai Zhang (Jilin University, LaSuN) and Prof Hong Xia, who helped me so lot during my stay in Jilin Univ. Prof. Zhang is an active man, who made me feel interesting to do research.

Prof. Katsumasa Fujita (Osaka University, LaSIE) and Prof. Storu Shoji, who helped me a lot for ordering materials for experiment and research discussion.

Jun Yu, Kazumasa Uetsuki, Kyoko Masui, Jun Ando, Almar F. Palonpon, Yoshito Okuno, Imad Maouli, Toshihiro Mino, Kozue Watanabe, Shota Ushiba, Yasuo Yonemaru, and Yoshiro Ohashi. They helped me a lot for imparting their knowledge and experiences on optics and photonics.

Ji-Hong Zhao, Xian-Bin Li, Ran Zhang, Yun-Lu Sun, Yan-Hao Yu, Yan-gang Bi, Ran Ding, Chun-Hao Li, Hao-Bo Jiang, Huan Wang, Bing Han and Zhuo-Chen Ma. They helped me a lot on imparting their knowledge on laser fabrication, and made my life in Jilin Univ. wonderful and happy.

By the end, thanks a lot for the people who supported me so lot, I wish you a nice life!